International Journal of Plasticity 47 (2013) 182–201

Contents lists available at SciVerse ScienceDirect

International Journal of Plasticity

journal homepage: www.elsevier.com/locate/ijplas

Homogenized constitutive and fatigue nucleation models from crystal plasticity FE simulations of Ti alloys, Part 1: Macroscopic anisotropic yield function

Somnath Ghosh [a,*], Masoud Anahid [b]

[a] Department of Civil Engineering, Johns Hopkins University, MD 21218, United States
[b] Department of Mechanical Engineering, The Ohio State University, OH 43210, United States

ARTICLE INFO

Article history:
Received 4 September 2012
Received in final revised form 11 December 2012
Available online 13 February 2013

Keywords:
Crystal plasticity
Anisotropic yield function
Titanium alloys
Homogenization
Sensitivity analysis

ABSTRACT

Deformation and fatigue failure behavior of polycrystalline titanium alloys have strong dependence on the local microstructural characteristics. Reliable analysis of mechanical response and fatigue life in structures is contingent upon accurate description of material behavior using continuum-level constitutive models, with roots in the underlying microstructure. This two part paper is aimed at developing continuum models of plastic deformation and fatigue crack nucleation in polycrystalline Ti alloys from detailed analysis of underlying polycrystalline microstructures. In the first of this two-part paper, a homogenized, anisotropic plasticity constitutive (HAPC) model is developed from crystal plasticity finite element simulation results of microstructural representative volume elements. This model is able to capture important deformation characteristics of Ti-based alloys, which are pressure insensitivity, anisotropy and tension–compression asymmetry. The advantage of this model is that it avoids having to perform computationally expensive micromechanical analysis at each point in macroscopic simulations. An extension of this model is also introduced to account for the rate dependency observed in mechanical behavior of Ti alloys. In the second part of this two-part paper, a macroscopic, probabilistic fatigue crack nucleation model is developed using the HAPC model.

1. Introduction

Titanium alloys find important utilization in various defense and commercial applications due to their high strength, low density, high fracture toughness and corrosion resistance. Plastic deformation in these predominantly hexagonal close-packed or *hcp* alloys has considerable dependence on the underlying microstructure, e.g. crystal orientation due to their low symmetries (Hasija et al., 2003; Deka et al., 2006; Venkataramani et al., 2006) and grain size (Venkatramani et al., 2007). Slip behavior due to dislocation glide in hexagonal materials is highly anisotropic because of the difference in deformation resistances for different slip systems. The critical resolved shear strength (CRSS) for ⟨c + a⟩-slip on the pyramidal planes is ∼3–4 times larger than the CRSS for ⟨a⟩-type slip on the prism or basal planes (Hasija et al., 2003). Under creep conditions "soft" grains with favorably oriented ⟨a⟩-type slip systems for dislocation glide (⟨c⟩-axis with nearly 45° orientation with respect to the deformation axis) undergo significant plastic straining. Contiguous "hard" grains with less-favorably oriented for ⟨a⟩-type slip (⟨c⟩-axis parallel to the deformation direction), experience large local stress concentrations, especially near the shared grain boundary.

* Corresponding author. Address: 3400 N. Charles St., Baltimore, MD 21218, United States. Tel.: +1 410 516 7833; fax: +1 410 516 7473.
E-mail address: sghosh20@jhu.edu (S. Ghosh).

0749-6419/$ - see front matter © 2013 Elsevier Ltd. All rights reserved.
http://dx.doi.org/10.1016/j.ijplas.2012.12.008

Prediction of deformation behavior and fatigue life in polycrystalline Ti alloys has received considerable attention within the materials research community in the recent times (see for e.g. Nixon et al., 2010; Fan and Yang, 2011; Khan et al., 2012). Significant research has been conducted to develop continuum plasticity models for titanium alloys, e.g. in Miller et al. (1999), Semiatin et al. (2002), and Khan et al. (2004, 2007). Based on phenomenological approaches, these macroscopic constitutive models introduce internal scalar or tensor variables that are typically determined from experimental observations. While these models have been undoubtedly very useful in structural scale analyses using computational methods like the finite element method, a shortcoming sometimes encountered is that they do not explicitly account for microstructural characteristics and evolving deformation mechanisms. Lack of adequate information on microstructural morphology and underlying physical mechanisms often result in limited predictive capabilities for general material and load classes. To compensate for this, some models have incorporated a large number of parameters in their expressions without direct physical relevance. Similarly, conventional fatigue analysis methods by, e.g., the stress-life or strain-life approaches, or damage tolerant approaches (Suresh, 1998) exhibit scatter in their predictions due to lack of underlying physics based mechanisms and information about the actual material microstructure. Material microstructure-based mechanistic models of deformation and fatigue failure is seen as a promising alternative to such empiricism. Crystal plasticity finite element (CPFE) models with explicit grain structures in polycrystalline aggregates have been developed for predicting localized stresses and plastic strains, e.g. in Balasubramanian and Anand (1996), Anand and Kothari (1996), Barbe et al. (2001a,b), Morrissey et al. (2003), Goh et al. (2003), Hasija et al. (2003), Deka et al. (2006), Venkataramani et al. (2006, 2007, 2008), Zhang et al. (2007), and Rossiter et al. (2010). These explicit microstructure-based CPFE models have been extended to model fatigue failure in Anahid et al. (2011), Sinha et al. (2004), Bache (2003), Sackett et al. (2007), Bridiera et al. (2009), and McDowell and Dunne (2010). It is however prohibitive to conduct computational modeling of the entire structure at the scale of the microstructure with explicit representation grains, especially for large domains.

Multi-scale computational homogenization theories have been proposed for estimating averaged material properties of heterogeneous materials (Terada and Kikuchi, 2001; Kouznetsova et al., 2001; Ghosh et al., 2001; Feyel and Chaboche, 2000; Paquet et al., 2011; Segurado et al., 2012; Watanabe et al., 2012). For crystal plasticity, this class of multi-scale finite element models for predicting anisotropy and texture evolution, assign a polycrystalline microstructure to each element integration point, whose texture evolves with time. In Wu et al. (2007), a uniform deformation gradient is enforced in all constituent grains of the polycrystalline microstructure according to Taylor's assumption, to predict anisotropic stress–strain response in high purity α Ti alloys. A polycrystalline model with self-consistent homogenization scheme is implemented in an explicit FE code in Tome et al. (2001) to simulate the mechanical response of textured zirconium, deforming under four-point bend conditions. These approaches however can be computationally intractable for large structural problems, since detailed micromechanical analyses should be conducted for every integration point of macroscopic elements in a finite element model.

To overcome the shortcomings of simultaneous macro–micro modeling, different techniques have been suggested to reduce prohibitive numerical efforts required for CPFE simulations. A reduced texture methodology (RTM) has been proposed in Rousselier et al. (2012) to provide the computational efficiency needed for macroscopic plasticity modeling of aluminum extrusions. This polycrystalline plasticity based approach involves a significant reduction of the number of representative crystallographic orientations. A special "texture-component crystal plasticity finite element" has been proposed in Raabe and Roters (2004) and Raabe et al. (2004) where the initial orientation distribution function (ODF) is approximated in the form of discrete localized spherical texture components at integration points of the FE mesh. Each preferred orientation is assigned a scatter and amplitude. While this scattering of discrete orientations prevents overestimation of the overall anisotropy, the local anisotropy is still overestimated (Bohlke et al., 2006). A promising alternative to incorporating crystal plasticity models in multi-scale finite element codes is to develop texture-based anisotropic yield surface models at the macroscopic level, e.g. in Cazacu and Barlat (2003, 2004), An et al. (2011), and Inal et al. (2010). Yield functions are expressed in terms of some polynomials whose coefficients are functions of microstructural properties. Selection of an appropriate yield function, which can capture important deformation characteristics is essential to get a dependable distribution of local stress/strains and reliable life prediction. For multi-phase materials undergoing damage and failure, Ghosh et al. have developed computationally efficient, anisotropic homogenization based continuum plasticity-damage (HCPD) in ductile–elastic–plastic materials (Ghosh et al., 2009) and homogenization based continuum damage mechanics (HCDM) in brittle–elastic composites (Jain and Ghosh, 2008). These reduced order models are constructed from rigorous homogenization of micromechanical analyses results of representative volume elements (RVE), following the Hill–Mandel postulate. These homogenized, reduced order models modify conventional phenomenological models to account for the presence of heterogeneities and their interactions in the microstructure. These aspects give rise to strong anisotropy in the constitutive relations that evolve with increasing plasticity and damage.

This two part paper is aimed at developing homogenization-based macroscopic constitutive and crack nucleation models from detailed micromechanical crystal plasticity FE analysis of polycrystalline microstructures. The first part develops a homogenized, anisotropic plasticity constitutive model, specifically a yield function, for Ti alloys in a vein similar to developments in Ghosh et al. (2009) and Jain and Ghosh (2008). This model can be incorporated in general purpose FEM codes for macroscopic analysis, thus avoiding computationally expensive polycrystalline micromechanical analysis at each integration point in a finite element mesh. The yield function proposed by Cazacu and Barlat (2001, 2003, 2004) possesses desired properties for modeling the anisotropic behavior of textured titanium alloys. It can also capture the tension–compression asymmetry inherent to these materials. This framework is adopted for the homogenized plasticity constitutive model for Ti alloys.

The model is further extended to accommodate rate-dependent behavior observed in these alloys. The second part develops a probabilistic crack nucleation model for structural scale analysis of polycrystalline Ti alloys from grain-level crack nucleation results.

In this paper, the crystal plasticity finite element model (CPFEM) for micro-level simulations is presented in Section 2. Section 3 provides a detailed discussion on sensitivity analysis, required for determining microstructural parameters that should be incorporated in the homogenized model. Homogenization of the crystal plasticity simulation results is performed in Section 4 to develop the continuum anisotropic constitutive models. Different anisotropic yield functions are discussed in this section for describing the mechanical behavior of Ti alloys. An extension to incorporate the rate sensitivity is discussed in Section 4.4.

2. Crystal plasticity finite element (CPFE) model for micro-scale polycrystalline simulations

Ti alloys are characterized by time-dependent "cold" creep deformation characteristics at temperatures lower than those, at which diffusion-mediated deformation such as dislocation climb is expected (Imam and Gilmore, 1979; Neeraj et al., 2000; Hasija et al., 2003). TEM studies (Neeraj et al., 2000) have shown that deformation actually proceeds via dislocation glide, and dislocations are inhomogeneously distributed into planar arrays. No evidence of twinning has been seen in these studies at room temperature. Additionally, the relatively high Al content in these materials ~6.5% inhibits the formation of twins (Williams et al., 2002) and hence twinning is not considered in the crystal plasticity models. Significant creep strains can accumulate at applied stresses, even as low as 60% of the yield strength. This characteristic has been attributed to rate effects in Imam and Gilmore (1979). The material studied in this work is single-phase α-Ti-6Al which has a *hcp* crystal structure. The *hcp* crystals consist of 5 different families of slip systems, namely the basal ⟨a⟩, prismatic ⟨a⟩, pyramidal ⟨a⟩, first order pyramidal ⟨c + a⟩ and second order pyramidal ⟨c + a⟩ with a total of 30 slip systems. Size and time dependent, finite strain CPFE models have been developed by Ghosh et. al. in Hasija et al. (2003), Deka et al. (2006), and Venkataramani et al. (2006, 2007, 2008).

In the CPFE model, crystal deformation results from a combination of the elastic stretching and rotation of the crystal lattice and plastic slip on the different slip systems. The stress–strain relation is written in terms of the second Piola–Kirchoff stress $\mathbf{S}$ and its work conjugate Lagrange–Green strain tensor $\mathbf{E}^e$ as

$$\mathbf{S} = \mathbf{C} : \mathbf{E}^e, \quad \text{where } \mathbf{E}^e = \frac{1}{2}(\mathbf{F}^{e^T}\mathbf{F}^e - \mathbf{I}) \tag{1}$$

$\mathbf{C}$ is a fourth order anisotropic elasticity tensor and $\mathbf{F}^e$ is the elastic component of the deformation gradient, obtained by multiplicative decomposition as:

$$\mathbf{F} = \mathbf{F}^e\mathbf{F}^p, \quad \det(\mathbf{F}^e) > 0 \tag{2}$$

where $\mathbf{F}$ is the deformation gradient tensor and $\mathbf{F}^p$ is its incompressible plastic component, i.e. $\det \mathbf{F}^p = 1$. The plastic part of the crystal plasticity equations involves a combined effect of slip on multiple slip systems. The flow rule, governing evolution of plastic deformation, is expressed in terms of the plastic velocity gradient $\mathbf{L}^p$ as:

$$\mathbf{L}^p = \dot{\mathbf{F}}^p\mathbf{F}^{p-1} = \sum_{\alpha}^{nslip} \dot{\gamma}^\alpha \mathbf{s}^\alpha \tag{3}$$

where the Schmid tensor associated with α-th slip system $\mathbf{s}^\alpha$ is expressed in terms of the slip direction $\mathbf{m}_0^\alpha$ and slip plane normal $\mathbf{n}_0^\alpha$ in the reference configuration as $\mathbf{s}^\alpha = \mathbf{m}_0^\alpha \otimes \mathbf{n}_0^\alpha$. The plastic slip rate $\dot{\gamma}^\alpha$ on the α-th slip system has a power law dependence on the resolved shear stress (τ^α) and the slip system deformation resistance (g^α), given as

$$\dot{\gamma}^\alpha = \dot{\bar{\gamma}}\left|\frac{\tau^\alpha - \chi^\alpha}{g^\alpha}\right|^{1/m} sign(\tau^\alpha - \chi^\alpha) \tag{4}$$

Here m is the material rate sensitivity parameter, $\dot{\bar{\gamma}}$ is the reference plastic shearing rate and χ^α is the back stress that accounts for kinematic hardening in cyclic deformation (Hasija et al., 2003).

The evolution of slip system deformation resistance is assumed to be controlled by two types of dislocations, viz. statistically stored dislocations (SSDs) and geometrically necessary dislocations (GNDs). SSD's correspond to homogeneous plastic deformation, while GND's accommodate incompatibility of the plastic strain field due to lattice curvature, especially near grain boundaries. The corresponding deformation resistance rate is expressed as:

$$\dot{g}^\alpha = \sum_\beta h^{\alpha\beta}|\dot{\gamma}^\beta| + \frac{k_0\hat{\alpha}^2G^2b}{2(g^\alpha - g_0^\alpha)}\sum_\beta \lambda^\beta|\dot{\gamma}^\beta| \tag{5}$$

The first term in Eq. (5) corresponds to SSDs. The modulus $h^{\alpha\beta} = q^{\alpha\beta}h^\beta$ (no sum on β) is the strain hardening rate due to self and latent hardening on the α-th slip system by slip on the β-th slip system respectively. Here, h^β is the self hardening coefficient and $q^{\alpha\beta}$ is a matrix describing latent hardening. The second term in Eq. (5) accounts for the effect of GNDs on work hardening (Acharya and Beaudoin, 2000). Here, k_0 is a dimensionless material constant, G is the elastic shear modulus, b is

the Burgers vector, g_0^α is the initial deformation resistance and $\hat{\alpha}$ is a non-dimensional constant. $\hat{\alpha}$ is taken to be $\frac{1}{3}$ in this work following (Ashby, 1970). λ^β is a measure of slip plane lattice incompatibility, which can be expressed for each slip system as a function of slip plane normal $\mathbf{n}^\beta$ and an incompatibility tensor Λ as:

$$\lambda^\beta = (\mathbf{\Lambda n}^\beta : \mathbf{\Lambda n}^\beta)^{\frac{1}{2}} \tag{6}$$

The dislocation density tensor Λ, introduced in Nye (1953) is a direct measure of the GND density. It can be expressed using the curl of plastic deformation gradient tensor $\mathbf{F}^P$. Since this crystal plasticity formulation does not explicitly incorporate a dislocation density tensor, it is indirectly extracted from the CPFE output data as:

$$\mathbf{\Lambda} = \nabla^T \times \mathbf{F}^P \tag{7}$$

Grain size has a significant effect on the initial deformation resistance g_0^α. A Hall–Petch type relation with various slip direction-dependent characteristic length scales has been incorporated in the CPFE model in Venkataramani et al. (2007, 2008). Material properties for each individual slip system in the crystal plasticity model, as well as size effect parameters have been calibrated in Hasija et al. (2003), Deka et al. (2006), and Venkataramani et al. (2006, 2007). Other parameters used in Eq. (5) include (i) shear modulus $G = 48$ GPa, (ii) magnitude of Burgers vector $b = 0.30$ nm, and (iii) $k_0 = 2$. Details of the morphological and crystallographic features of the microstructures are also accounted for in the CPFE model through accurate grain size and orientation distributions. Extensive developments on polycrystalline microstructures that are statistically equivalent to those observed in OIM scans have been made in Ghosh et al. (2008) and Groeber et al. (2008a,b).

3. Sensitivity analysis with respect to microstructural parameters

Prior to developing a microstructure-dependent, macroscopic constitutive model for the Ti alloy α-Ti-6Al, sensitivity analysis is conducted to assess the dependence of material response on important features pertaining to the underlying microstructure. The macroscopic response is established by homogenizing the CPFE simulation results for the polycrystalline microstructural representative volume elements (RVEs). It is also essential to establish critical parameters that adequately characterize the polycrystalline microstructure, which can be incorporated in the model.

3.1. Parameters representing microstructural characteristics

Four different parameters, which represent crystallographic and morphological characteristics of the microstructure are considered for the sensitivity analysis. These are delineated in the following sub-sections.

3.1.1. Orientation distribution function (ODF)

Plastic deformation in *hcp* crystalline Ti alloys has considerable dependence on the crystal orientation due to their low symmetries. The deformation resistance g^α for the ⟨c + a⟩ slip on pyramidal planes is ∼3–4 times larger than that for ⟨a⟩-type slip on prism or basal planes (Hasija et al., 2003). This implies that plastic deformation in polycrystalline Ti alloys is primarily the result of slip activity on the basal and prismatic slip system in grains with the highest value of the critical resolved shear stress τ^α. The Schmid factor (*SF*), for a slip system α depends on the loading axis and is defined as:

$$SF = \cos\phi \cos\lambda \tag{8}$$

where ϕ is the angle between the loading axis and the slip plane normal $\mathbf{n}^\alpha$, and λ is the angle between loading axis and the slip direction $\mathbf{m}^\alpha$ in the reference configuration. The *SF* transforms the applied stress to the resolved shear stress on a given slip system. Therefore, corresponding to Eq. (4), the *SF* of each slip system in a grain has a direct effect on the plastic behavior of that grain, and consequently on the overall plastic response of the microstructure. In this study the *SF* for each grain will henceforth correspond to the highest Schmid factor among basal and prism slip systems in the grain. A grain with considerable plastic deformation is termed as a "soft" grain. Softer grains in a microstructure have higher values of *SF* in comparison with other grains. To represent the orientation of slip systems in each grain with respect to the three orthogonal reference axes x, y, z, three Schmid factor components labeled as SF_x, SF_y and SF_z are defined for x, y and z directed loadings, respectively. The distribution of SF_x, SF_y and SF_z is considered as a good representation of the orientation of a polycrystalline microstructure. The average values of each of these distributions for each component, are considered as scalar measures of the orientation that can be incorporated in the constitutive relation. Fig. 1 shows the distribution of SF_x, SF_y and SF_z for a sample microstructure containing 600 grains labeled as MS1. The average values of these component parameters are $\overline{SF}_x = 0.405$, $\overline{SF}_y = 0.425$ and $\overline{SF}_z = 0.441$.

3.1.2. Misorientation distribution function (MoDF)

The misorientation between two neighboring grains 1 and 2 is measured in terms of a rotation axis vector $\mathbf{n}$ and a misorientation angle θ_{mis} (Deka et al., 2006). The axis $\mathbf{n}$ represents a common slip direction for both crystallographic lattice systems. The misorientation angle θ_{mis} between two neighboring grains is the rotation about $\mathbf{n}$, required to bring the two crystal lattices into coincidence, and is expressed as:

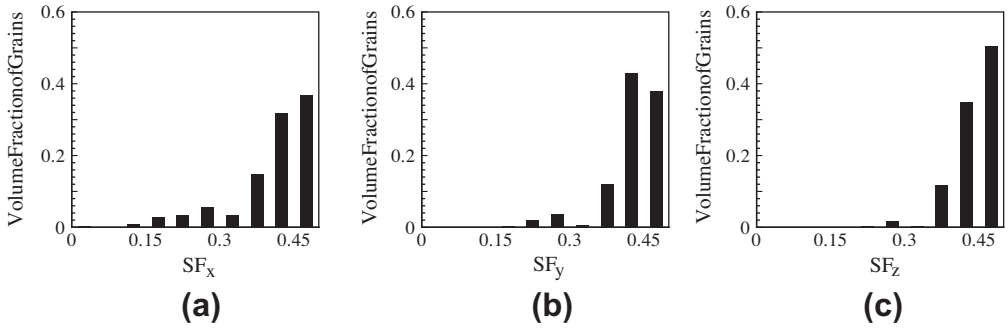

Fig. 1. Distribution functions of the three components of Schmid factor for a microstructure labeled MS1: (a) SF_x, (b) SF_y, and (c) SF_z.

$$\theta_{\text{mis}} = \min \left| \cos^{-1} \left[\frac{\text{tr}(\mathbf{g}_1 \mathbf{g}_2^{-1} \mathbf{O} - \mathbf{I})}{2} \right] \right| \tag{9}$$

where $\mathbf{g}_1$ and $\mathbf{g}_2$ represent orientation matrices of grain 1 and 2, respectively and $\mathbf{O}$ is a crystal symmetry operator defined in Deka et al. (2006). Three scalar parameters are used to represent the misorientation distribution (MoDF) in macroscopic constitutive relations, viz. (i) mean (μ_{MoDF}), (ii) standard deviation (σ_{MoDF}), and (iii) percentage of grain pairs with misorientation less than 20° (R_{MoDF}).

3.1.3. Texture distribution function (TDF)

A parameter, termed as "texture index" or *TI* is defined for each grain as the volume fraction of its neighboring grains with similar orientation. A neighbor is considered to have similar orientation as the central grain, if the misorientation angle between the two grains is less than 15°. The parameter *TI* values range from 0 to 1. For all grains in the microstructure having the same orientation, the *TI* is 1 for all grains. On the other hand, $TI \to 0$ for all grains, in a purely random microstructure. It should be noted that the orientation of a textured region also affects the material macroscopic response. For example, a microstructure containing a large number of "hard" grains has a higher yield strength in comparison with that containing "soft" textured grains. To account for this, a modified texture index $\hat{TI}$ is defined as $TI \times SF$, where *SF* is the Schmid factor of that grain. $\hat{TI}$ ranges from 0 to 0.5. The distribution function of $\hat{TI}$ is considered as a representative of texturing and is denoted as TDF. Three scalar parameters are used to represent the texture distribution (TDF) in macroscopic constitutive relations, viz. (i) mean (μ_{TDF}), (ii) standard deviation (σ_{TDF}), and (iii) percentage of grains with $\hat{TI} \geqslant 0.25$ (R_{TDF}).

3.1.4. Grain size distribution function (GSDF)

The mechanical behavior of polycrystalline Ti alloys, in particular strength, has a strong dependence on grain size (Venkataramani et al., 2007). The strengthening effect is primarily due to dislocation pile-up at the grain boundary. The slip system deformation resistance is strongly affected by the mean free path traversed by dislocations. In Venkataramani et al. (2007), size effect is incorporated in the rate-dependent crystal plasticity constitutive model through insertion of characteristic length scales in the expression for deformation resistance of individual slip systems. For primary α grains, the characteristic length scale corresponds to the grain size, that is represented by the diameter of an equivalent sphere with the same volume as the grain. The grain size distribution in Ti alloys is found to follow a log-normal distribution, and hence the GSDF is assumed to be a log-normal function. This distribution function is defined by specifying the mean (μ_{GSDF}) and the standard deviation (σ_{GSDF}), which represent grain size distribution in the macroscopic constitutive relations.

3.1.5. Adequacy of the microstructural characteristic functions with respect to key mechanical properties

The four microstructural parameters and their distributions described in the previous sections should in general be sufficient to unambiguously represent the material response, at least with respect to key mechanical properties. Only then, can these be incorporated in the constitutive relations with confidence. To test this condition, different specimen virtual microstructures are generated using identical statistical distributions of the four parameters. While a few virtual samples have been tested, detailed discussions are provided for only two microstructures labeled as MS1 and MS2. MS1 consists of 600 grains, discretized into a FE mesh containing 124,820 tetrahedron elements, while MS2 has 500 grains with 102,697 tetrahedron elements, as shown in Fig. 2(a). Crystal plasticity FE simulations of the two microstructures are conducted by applying a tensile constant strain-rate of 10^{-4} s^{-1} in the x, y and z directions. The volume-averaged stress–strain response in these directions are respectively plotted in Fig. 2(b). The yield strength in each direction is obtained by applying the 0.2% offset rule on the resulting stress–strain curve as shown in Fig. 2(b). Table 1 summarizes the average Schmid factors and the evaluated yield strengths in the three directions for the two microstructures. The yield strength along the z direction is smaller in comparison with the other two directions, which is consistent with the observation that lower average value of Schmid factors correspond to higher yield strength. For the same loading conditions, the maximum difference in yield strength between the

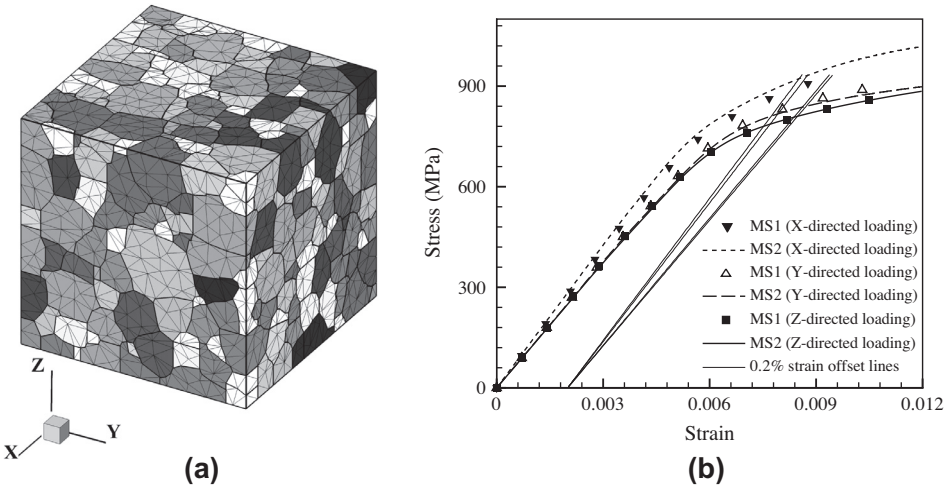

Fig. 2. (a) A virtual microstructure of MS2 with 500 grains, discretized into 102,697 tetrahedron elements and (b) stress–strain curves for microstructures MS1 and MS2 corresponding to x, y and z-directed strain loadings.

Table 1
Average Schmid factors and yield strengths of microstructural specimens MS1 and MS2 in the x, y and z directions.

	Average Schmid factors			Yield stress (MPa)		
	$\overline{SF}x$	$\overline{SF}y$	$\overline{SF}z$	x-Direction loading	y-Direction loading	z-Direction loading
MS1	0.405	0.425	0.441	897	852	826
MS2	0.405	0.425	0.441	922	840	812

two microstructures with same statistics is found to be 2.7%. This small difference in response establishes the conjecture that the four parameters adequately represent the key material response.

3.2. Sensitivity of macroscopic response to microstructural parameters

Sensitivity of the macroscopic stress–strain response to the microstructural parameters discussed in Section 3.1 is now analyzed. The macroscopic response is assumed to be characterized by three quantities, viz. (i) elastic stiffness E corresponding to the slope of the elastic portion; (ii) yield strength YS corresponding to 0.2% offset rule; and (iii) hardness H corresponding to the slope of stress–strain curve in the plasticity region. The difference in macroscopic responses of the two microstructures MS1 and MS2 is assumed to be negligible if the difference in E and YS are less than 4%, and the difference in H is less than 20% for the two microstructures. A higher tolerance is allowed for H to accommodate for its relatively small value in comparison with E. To substantiate this, Fig. 3 depicts the different stress–strain curves for the same values of yield strength ($YS = 936$ MPa) and elastic stiffness ($E = 117$ GPa), but different values of H. The 20% difference in H does not make a significant difference in the stress–strain curve.

3.2.1. Sensitivity of macroscopic response to TDF and MoDF

Two sets of virtual microstructures, containing $7 \times 7 \times 7$ cubic grains of equal size 7.5 μm each, are generated for this sensitivity analysis. The first set contains microstructures labeled MS3 and MS4, which have the same average Schmid factors ($\overline{SF}_x = 0.417, \overline{SF}_y = 0.434$ and $\overline{SF}_z = 0.452$). The virtual specimens are subjected to a tensile constant strain-rate of 10^{-4} s^{-1} in the y direction. The distributions of MoDF and TDF for MS3 and MS4 are presented in Figs. 4. The ordinates correspond to the grain contact area and volume fractions respectively, while the abscissae correspond to the misorientation angle and the texture index respectively. The distributions for the two microstructures are quite different. The values of the statistical metrics μ_{MoDF}, σ_{MoDF}, R_{MoDF}, and μ_{TDF}, σ_{TDF} and R_{TDF} are summarized in Table 2. The corresponding values of YS, H and E are also compared in this table. The percentage difference between the values of YS, H and E is 3.5, 5.8 and 0.5 respectively, which are all less than the tolerances assigned.

The second set of virtual microstructures considers three specimens labeled MS5, MS6 and MS7, all of which have the same average Schmid factors $\overline{SF}_x = 0.434$, $\overline{SF}_y = 0.418$ and $\overline{SF}_z = 0.428$. The corresponding TDF and MoDF plots are shown in Fig. 5. The values of the statistical metrics μ_{MoDF}, σ_{MoDF}, R_{MoDF}, μ_{TDF}, σ_{TDF} and R_{TDF}, along with the values of E, YS and H are summarized in Table 3. Again, the difference between the values of YS, H and E are less than the tolerances. Therefore

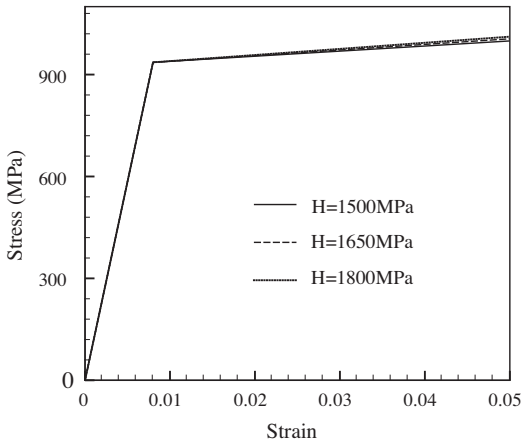

Fig. 3. Sensitivity of the stress–strain curve to the hardness H for constant $E = 117$ GPa, $YS = 936$ MPa.

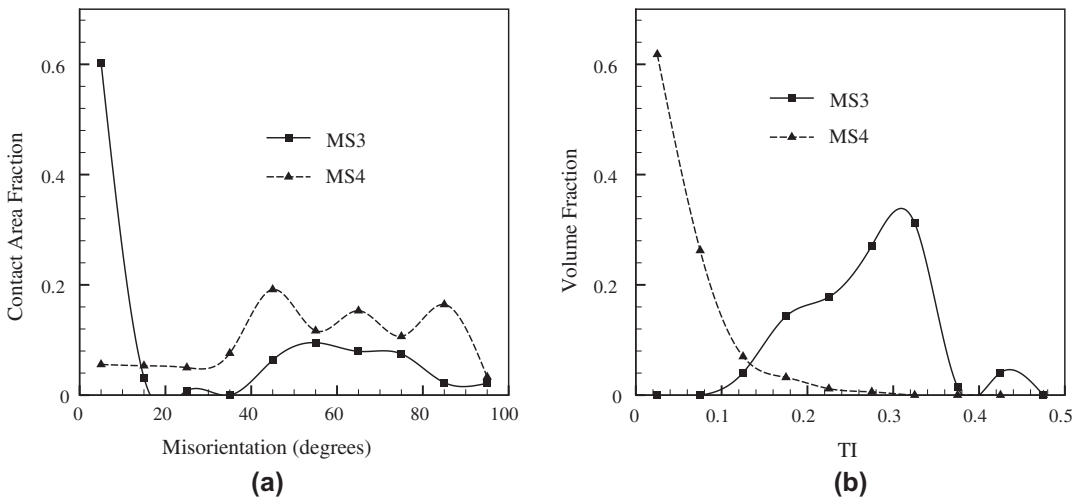

Fig. 4. Distribution of (a) MoDF represented by the misorientation angle, and (b) TDF represented by the texture index TI for virtual specimens MS3 and MS4.

Table 2
Parameters reflecting the mechanical response (stress–strain response) and distribution of MoDF and TDF in the microstructures of the virtual specimens MS3 and MS4.

	E (MPa)	YS (MPa)	H (GPa)	MoDF			TDF		
				μ_{MoDF}	σ_{MoDF}	R_{MoDF}	μ_{TDF}	σ_{TDF}	R_{TDF}
MS3	117	824	979	25.05	30.52	0.63	0.27	0.06	0.64
MS4	118	854	1038	54.92	24.17	0.11	0.04	0.06	0.01
Diff. (%)	0.5	3.5	5.8						

TDF and MoDF are inferred to have little effect on the macroscopic response. Moreover these parameters are considered to cause stress and strain redistribution between grains in the microstructure and are important in local phenomena like crack nucleation. The misorientation and texture parameters are consequently not included in the macroscopic constitutive model.

3.2.2. Sensitivity to the grain size distribution GSDF

A log-normal distribution of the GSDF is characterized by its mean μ_{GSDF} and standard deviation σ_{GSDF}. For sensitivity analysis of the macroscopic response to σ_{GSDF}, two virtual microstructures labeled MS8 and MS9 are generated with the same

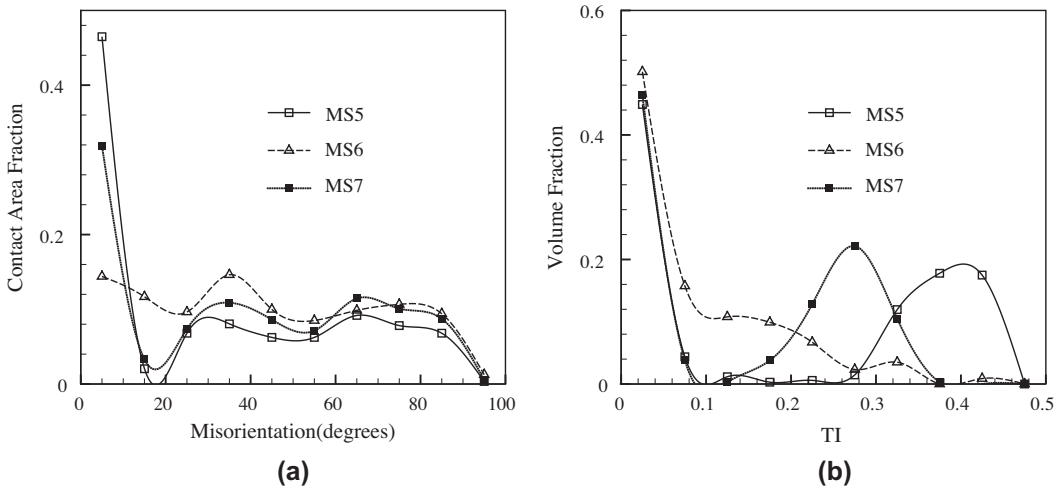

Fig. 5. Distribution of (a) MoDF represented by the misorientation angle, and (b) TDF represented by the texture index *TI* for virtual specimens MS5, MS6 and MS7.

Table 3
Parameters reflecting the mechanical response (stress–strain response) and distribution of MoDF and TDF in the microstructures of the virtual specimens MS5, MS6 and MS7.

	E (MPa)	YS (MPa)	H (GPa)	MoDF			TDF		
				μ_{MoDF}	σ_{MoDF}	R_{MoDF}	μ_{TDF}	σ_{TDF}	R_{TDF}
MS5	115	855	1065	30.45	29.99	0.49	0.19	0.18	0.49
MS6	115	861	1121	42.74	26.77	0.26	0.08	0.10	0.07
MS7	115	858	996	37.20	30.51	0.35	0.14	0.14	0.33
Max. diff. (%)	0.2	0.6	11.8						

average Schmid factor in all directions. The microstructures have the same average grain size i.e. $\mu_{GSDF} = 1$, but different standard deviations, viz. 0.486 for MS8 and 0.2 for MS9. Fig. 6(a) shows the GSDF for MS8 and MS9. Crystal plasticity FE simulations are conducted on the microstructures by applying a tensile constant strain rate of 10^{-4} s^{-1} in the y direction. The simulated macroscopic stress–strain curves are shown in Fig. 6(b). The corresponding yield strengths are $YS = 838.5$ MPa for MS8 and $YS = 892.9$ MPa for MS9. The difference in the two yield strengths is 6.1%, which is larger than the assumed tolerance of 4%. This difference can be explained as follows. Though both microstructures have the same average grain size, MS9

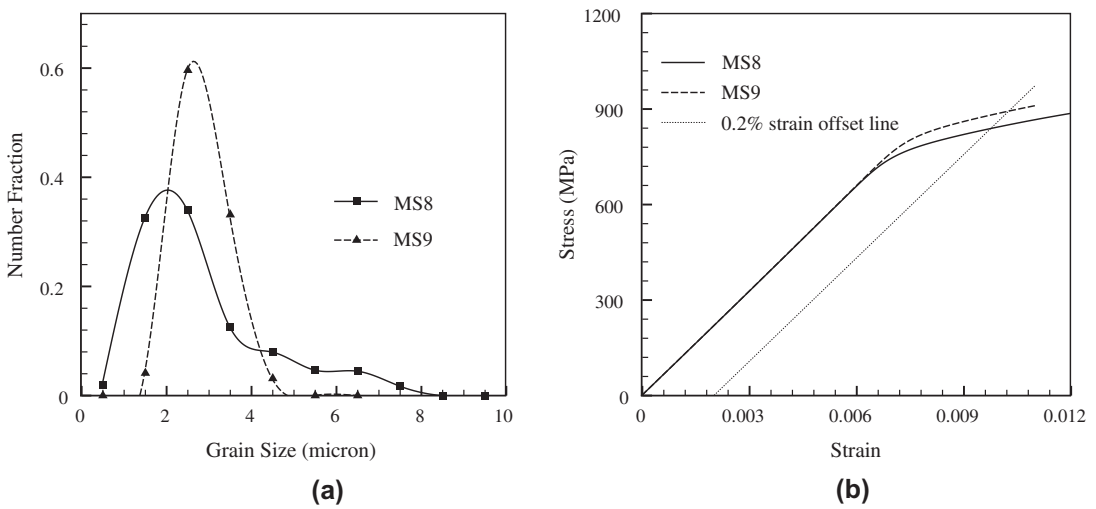

Fig. 6. (a) Distribution of grain size GSDF and (b) macroscopic stress–strain response for MS8 and MS9.

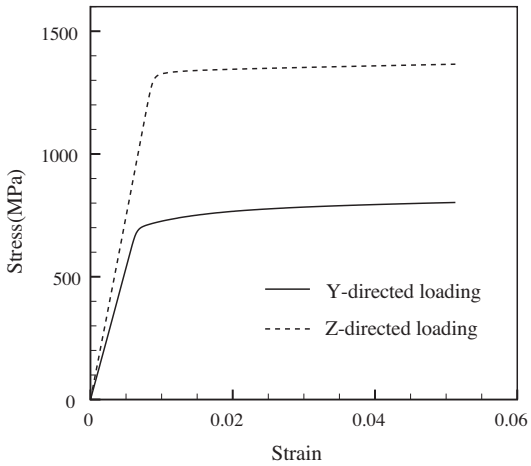

Fig. 7. Macroscopic stress–strain curves in the *y*- and *z*-directions.

Table 4
Stress–strain curve parameters for microstructure MS10 in the *y*- and *z*-directions.

	Schmid factor	*E* (GPa)	*YS* (MPa)	*H* (MPa)
y-Direction loading	0.47	106	718	918
z-Direction loading	0.15	148	1332	702
Diff. (%)		33.1	59.9	26.7

with higher σ_{GSDF} has a few number of very large grains. While the number fraction of these grains is small, the volume fraction of these grains is appreciable. Because the macroscopic response is obtained using volume averaging, the effect of these grains is important. The volume average of grain sizes for specimens MS8 and MS9 are 5.16 μm and 2.55 μm respectively. Consequently the parameter to be incorporated in constitutive relations is changed to the average of grain size distribution GSDF based on the volume fraction of grains. This is denoted by *D*.

3.2.3. Sensitivity of macroscopic response to ODF

Finally, the sensitivity of macroscopic response to the average Schmid factor is studied through CPFE simulations of a microstructure labeled MS10 that is soft in the *y* direction ($\overline{SF}_y = 0.47$) and hard in the *z* direction ($\overline{SF}_z = 0.15$). Two CPFE simulations are conducted with: (i) a tensile constant strain rate of 10^{-4} s^{-1} applied in the *y*-direction, and (ii) a tensile constant strain rate of 10^{-4} s^{-1} applied in the *z*-direction. Fig. 7 shows the macroscopic stress–strain curves for the *y*- and *z*-direction loadings. The values of E, YS and H for these two directions are given in Table 4. The values in the *y*- and *z*-directions differ considerably, requiring the insertion of the average Schmid factors in the constitutive models.

4. Development of homogenization-based anisotropic plasticity constitutive (HAPC) model for Ti alloys

The homogenization based continuum anisotropic plasticity or HAPC model is developed from micromechanical analysis of polycrystalline microstructures discussed previously. Specifically an appropriate yield function for the HAPC model is determined to capture the characteristics observed in mechanical behavior of Ti alloys.

4.1. Choice of a suitable framework for yield function

A few key features are necessary for selecting the suitable continuum yield criterion. These are: (i) pressure insensitivity, (ii) anisotropy, and (iii) tension–compression asymmetry. A few candidate anisotropic yield criteria are considered for this purpose. The quadratic anisotropic yield criterion for plastic deformation, described in Hill (1948), has a functional form in terms of the principal stress components as:

$$F(\sigma_1 - \sigma_2)^2 + G(\sigma_1 - \sigma_3)^2 + H(\sigma_2 - \sigma_3)^2 - Y_f^2 = 0 \tag{10}$$

where F, G and H are anisotropic parameters and Y_f is the flow stress. This model has been utilized mostly to model cubic metals that do not exhibit tension–compression asymmetry. Thus it is not suitable criterion for modeling Ti alloys with *hcp*

crystalline structure. This yield function has been modified in Hosford (1966) to account for tension–compression asymmetry by adding linear stress terms as:

$$F(\sigma_1-\sigma_2)^2+G(\sigma_1-\sigma_3)^2+H(\sigma_2-\sigma_3)^2+L\sigma_1+M\sigma_2-(L+M)\sigma_3-Y_f^2=0 \tag{11}$$

This function corresponds to a low eccentricity elliptical yield locus. However, this criterion is not suitable for modeling the highly anisotropic behavior of Ti alloys, which requires including higher order stress terms. A robust model for yielding and plastic deformation of anisotropic *hcp* materials has been proposed in Cazacu and Barlat (2003, 2004). The yield criterion is of the form:

$$(J_2^0)^{\frac{3}{2}}-J_3^0-Y_f^3=0 \tag{12}$$

where Y_f is the yield stress in shear. J_2^0 and J_3^0 are generalizations of the 2nd and 3rd invariants of the deviatoric stress tensor (J_2 and J_3) for orthotropy. They have been developed within the framework of the theory of representation of tensor functions in Cazacu and Barlat (2004). J_2^0 is expressed as:

$$J_2^0=\frac{a_1}{6}(\sigma_{xx}-\sigma_{yy})^2+\frac{a_2}{6}(\sigma_{xx}-\sigma_{zz})^2+\frac{a_3}{6}(\sigma_{yy}-\sigma_{zz})^2+a_4\sigma_{xy}^2+a_5\sigma_{xz}^2+a_6\sigma_{yz}^2 \tag{13}$$

J_3^0 is expressed as:

$$\begin{aligned}J_3^0=&\frac{1}{27}(b_1+b_2)\sigma_{xx}^3+\frac{1}{27}(b_3+b_4)\sigma_{yy}^3+\frac{1}{27}[2(b_1+b_4)-(b_2+b_3)]\sigma_{zz}^3+\frac{2}{9}(b_1+b_4)\sigma_{xx}\sigma_{yy}\sigma_{zz}-\frac{1}{9}(b_1\sigma_{yy}+b_2\sigma_{zz})\sigma_{xx}^2\\&-\frac{1}{9}(b_3\sigma_{zz}+b_4\sigma_{xx})\sigma_{yy}^2-\frac{1}{9}[(b_1-b_2+b_4)\sigma_{xx}+(b_1-b_3+b_4)\sigma_{yy}]\sigma_{zz}^2+2b_{11}\sigma_{xy}\sigma_{xz}\sigma_{yz}-\frac{1}{3}\sigma_{yz}^2[(b_6+b_7)\sigma_{xx}-b_6\sigma_{yy}\\&-b_7\sigma_{zz}]-\frac{1}{3}\sigma_{xz}^2[2b_9\sigma_{yy}-b_8\sigma_{zz}-(2b_9-b_8)\sigma_{xx}]-\frac{1}{3}\sigma_{xy}^2[2b_{10}\sigma_{zz}-b_5\sigma_{yy}-(2b_{10}-b_5)\sigma_{xx}]\end{aligned} \tag{14}$$

The number of anisotropic parameters in Eq. (12) is 17, which includes a_i ($i=1,2,\ldots,6$) and b_i ($i=1,2,\ldots,11$). If all coefficients b_i ($i=1,2,\ldots,11$) are set to zero, the Cazacu–Barlat or *C–B* criterion reduces to the Hill's model. J_3^0 with stress terms of odd exponents ensures that the *C–B* criterion of Eq. (12) takes into account the tension–compression asymmetry. For isotropic conditions $a_i=a_j$ ($i,j=1,2,\ldots,6$) and $b_i=b_j$ ($i,j=1,2,\ldots,11$). Both J_2^0 and J_3^0 do not depend on the hydrostatic stress, thus making the model pressure-insensitive. This model framework with higher order stress terms is examined for its suitability in representing the highly anisotropic behavior of Ti alloys.

4.2. Suitability of the Cazacu–Barlat framework for the HAPC model of Ti alloys

The sensitivity analysis in Section 3.2 concluded that four microstructural descriptor-based parameters, viz. the three orientation-related parameters ($\overline{SF}_x$, $\overline{SF}_y$ and $\overline{SF}_z$) and the volume averaged grain size D, should be incorporated in the three-dimensional HAPC model. The HAPC model for Ti alloys adopts the framework of the anisotropic yield function in Cazacu and Barlat (2001, 2003, 2004) with 17 anisotropic parameters in Eqs. (12)–(14). The model parameters are calibrated by homogenization of CPFE micromechanical analyses conducted on representative volume elements (RVE) of the microstructure with different microstructural features. They are naturally functions of the microstructure descriptors, and may evolve with increasing plastic flow as deduced in Section 4.3. The homogenized flow stress in shear in Eq. (12) is a function of the microstructural descriptors as well as the macroscopic plastic work. The material principal coordinate system introduced in Ghosh et al. (2009) is accounted for by representing RVEs in terms of orientation-dependent descriptors $\overline{SF}_x$, $\overline{SF}_y$ and $\overline{SF}_z$.

To examine the suitability of the *C–B* yield criterion in capturing the anisotropic behavior of Ti alloys, numerical simulations are conducted for the RVE labeled M10 with a strong micro-texture, characterized by the distribution descriptors $\overline{SF}_x=0.471$, $\overline{SF}_y=0.470$, $\overline{SF}_z=0.146$ and $D=7.5$ μm. M10 consists of $7\times7\times7$ cubic grains, discretized into a FE mesh of 16464 tetrahedron elements. The RVE is subjected to 19 loading conditions delineated below.

- Three uniaxial tension tests along x, y and z directions.
- Three pure shear tests on xy, xz and yz planes.
- Three uniaxial compression tests along x, y and z directions.
- Three biaxial tension tests ($\epsilon_{xx}:\epsilon_{yy}=1:1$ with $\sigma_{zz}=0$; $\epsilon_{zz}:\epsilon_{xx}=1:1$ with $\sigma_{yy}=0$; and $\epsilon_{yy}:\epsilon_{zz}=1:1$ with $\sigma_{xx}=0$).
- Three biaxial compression tests ($\epsilon_{xx}:\epsilon_{yy}=-1:-1$ with $\sigma_{zz}=0$; $\epsilon_{zz}:\epsilon_{xx}=-1:-1$ with $\sigma_{yy}=0$; and $\epsilon_{yy}:\epsilon_{zz}=-1:-1$ with $\sigma_{xx}=0$).
- Four tension tests with constrained transverse strain ($\epsilon_{xx}:\epsilon_{zz}=1:0$ with $\sigma_{yy}=0$; $\epsilon_{xx}:\epsilon_{yy}=1:0$ with $\sigma_{zz}=0$; $\epsilon_{yy}:\epsilon_{zz}=1:0$ with $\sigma_{xx}=0$; and $\epsilon_{xx}:\epsilon_{zz}=0:1$ with $\sigma_{yy}=0$).

Since Y_f is the homogenized flow stress in shear, CPFE simulation of simple shear test in the xy plane is used to calculate Y_f. Micromechanical analysis is followed by homogenization. The macroscopic plastic work W_p and Cauchy stress components σ_{ij} are evaluated from the microstructural variables using the relations:

$$W_p = \frac{1}{V}\sum_{I=1}^{N^e} W_p^I V^I \quad \text{and} \quad \sigma_{ij} = \frac{1}{V}\sum_{I=1}^{N^e} \sigma_{ij}^I V^I \tag{15}$$

where W_p^I and σ_{ij}^I are the plastic work and stress components at integration points of the tetrahedral element I, V^I is the volume of the Ith element and V is the total volume of the microstructure. For pure shear loading in the xy plane, the only non-zero macroscopic stress component is σ_{xy}. Therefore Eqs. (12)–(14) reduce to

$$(a_4)^{\frac{3}{2}}\sigma_{xy}^3 - Y_f^3 = 0 \tag{16}$$

Parameter a_4 is set to 1 to make $Y_f(W_p) = \sigma_{xy}$. The flow stress Y_f is plotted as a function of W_p in Fig. 8(a).

4.2.1. Yield surface with calibrated parameters in the C–B model framework

To calibrate the anisotropic parameters a_i $(i = 1, 2, 3, 5, 6)$ and b_i $(i = 1, 2, \ldots, 11)$, CPFE simulations are performed for RVE-M10 under the 19 loading conditions, followed by homogenization. All loading conditions are prescribed for a constant strain-rate of $10^{-4}\ s^{-1}$. At the end of each strain increment in the CPFE analyses, macroscopic stresses and plastic work are obtained from Eq. (15). The stress components are plotted as functions of W_p in Fig. 8(b), for one of the biaxial tension loadings $\epsilon_{yy} : \epsilon_{zz} = 1 : 1$ under plane stress conditions ($\sigma_{xx} = 0$). The macroscopic normal stress σ_{yy} is much less than σ_{zz} due to anisotropy of this microstructure. For a given value of W_p, the stress components are obtained from plots such as in Fig. 8(b). This is done for all the loading conditions. The anisotropic parameters are then evaluated by least square minimization of function in Eq. (12) as:

$$\min_{a_i(i=1,\ldots,6),b_i(i=1,\ldots,11)} \sum_{I=1}^{19} [(J_2^0)_I^{3/2} - (J_3^0)_I - Y_f^3]^2 \tag{17}$$

Here

$$(J_2^0)_I = \frac{a_1}{6}(\sigma_{xx}^I - \sigma_{yy}^I)^2 + \frac{a_2}{6}(\sigma_{xx}^I - \sigma_{zz}^I)^2 + \frac{a_3}{6}(\sigma_{yy}^I - \sigma_{zz}^I)^2 + a_4(\sigma_{xy}^I)^2 + a_5(\sigma_{xz}^I)^2 + a_6(\sigma_{yz}^I)^2 \tag{18}$$

and

$$\begin{aligned}(J_3^0)_I = {} & \frac{1}{27}(b_1+b_2)(\sigma_{xx}^I)^3 + \frac{1}{27}(b_3+b_4)(\sigma_{yy}^I)^3 + \frac{1}{27}[2(b_1+b_4)-(b_2+b_3)](\sigma_{zz}^I)^3 + \frac{2}{9}(b_1+b_4)\sigma_{xx}^I\sigma_{yy}^I\sigma_{zz}^I \\ & - \frac{1}{9}(b_1\sigma_{yy}^I + b_2\sigma_{zz}^I)(\sigma_{xx}^I)^2 - \frac{1}{9}(b_3\sigma_{zz}^I + b_4\sigma_{xx}^I)(\sigma_{yy}^I)^2 - \frac{1}{9}[(b_1-b_2+b_4)\sigma_{xx}^I + (b_1-b_3+b_4)\sigma_{yy}^I](\sigma_{zz}^I)^2 \\ & + 2b_{11}\sigma_{xy}^I\sigma_{xz}^I\sigma_{yz}^I - \frac{1}{3}(\sigma_{yz}^I)^2[(b_6+b_7)\sigma_{xx}^I - b_6\sigma_{yy}^I - b_7\sigma_{zz}^I] - \frac{1}{3}(\sigma_{xz}^I)^2[2b_9\sigma_{yy}^I - b_8\sigma_{zz}^I - (2b_9-b_8)\sigma_{xx}^I] \\ & - \frac{1}{3}(\sigma_{xy}^I)^2[2b_{10}\sigma_{zz}^I - b_5\sigma_{yy}^I - (2b_{10}-b_5)\sigma_{xx}^I]\end{aligned} \tag{19}$$

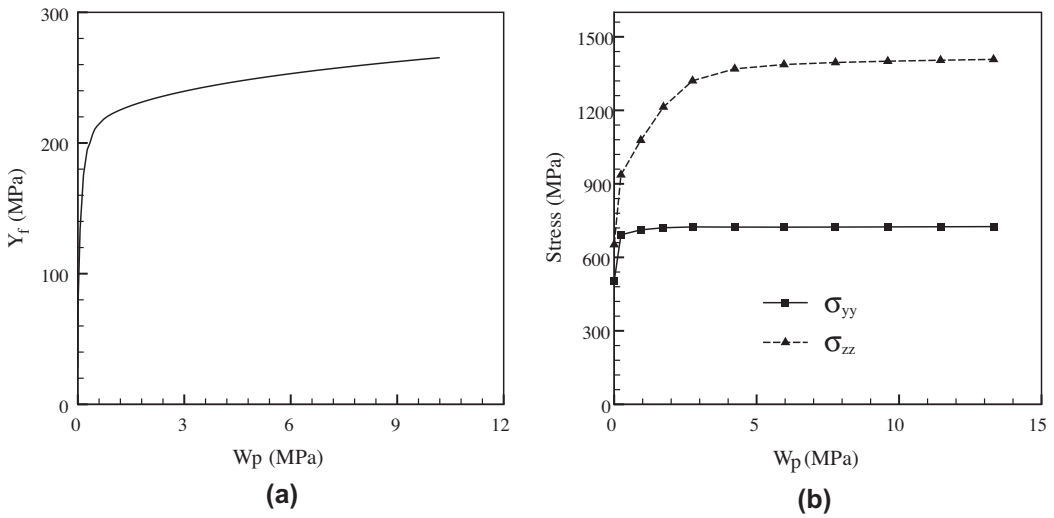

Fig. 8. Homogenized response parameters plotted as a function of macroscopic plastic work: (a) flow stress obtained from pure shear loading in the xz plane and (b) stress components for the biaxial tension loading $\epsilon_{yy} : \epsilon_{zz} 1 : 1$ under plane stress conditions ($\sigma_{xx} = 0$).

In Eqs. (18) and (19), σ_{ij}^{I} are the macroscopic stress components for the loading case number I at a given value of W_p. After evaluating the anisotropic parameters for a given value of W_p, the 3D yield locus in the principal coordinate system can be obtained from Eqs. (12)–(14) by setting the shear stress components to zero. This results in:

$$\left[\frac{a_1}{6}(\sigma_1-\sigma_2)^2+\frac{a_2}{6}(\sigma_1-\sigma_3)^2+\frac{a_3}{6}(\sigma_2-\sigma_3)^2\right]^{\frac{3}{2}}-\left\{\frac{1}{27}(b_1+b_2)\sigma_1^3+\frac{1}{27}(b_3+b_4)\sigma_2^3+\frac{1}{27}[2(b_1+b_4)-(b_2+b_3)]\sigma_3^3+\frac{2}{9}(b_1+b_4)\sigma_1\sigma_2\sigma_3-\frac{1}{9}(b_1\sigma_2+b_2\sigma_3)\sigma_1^2-\frac{1}{9}(b_3\sigma_3+b_4\sigma_1)\sigma_2^2-\frac{1}{9}[(b_1-b_2+b_4)\sigma_1+(b_1-b_3+b_4)\sigma_2]\sigma_3^2\right\}-Y_f^3=0 \tag{20}$$

where σ_1, σ_2 and σ_3 are the principal stresses. The 3D yield locus for the microstructure M10 at $W_p = 0.1$ MPa is shown in Fig. 9(a). The projection of this yield surface on the $\sigma_1 - \sigma_3$ plane is compared with numerical data obtained from CPFE simulations in Fig. 9(b). Good agreement is observed between the *C–B* yield locus and the stress data-points obtained from CPFE simulations. Evolution of the yield locus with increase in plastic work ($W_p = 0.1$, 1.0, 4.0 and 10.0 MPa) is shown in Fig. 9(c). Values of the anisotropic parameters in Eq. (20), corresponding to $W_p = 0.1$ MPa are summarized in Table 5. The values of b_i

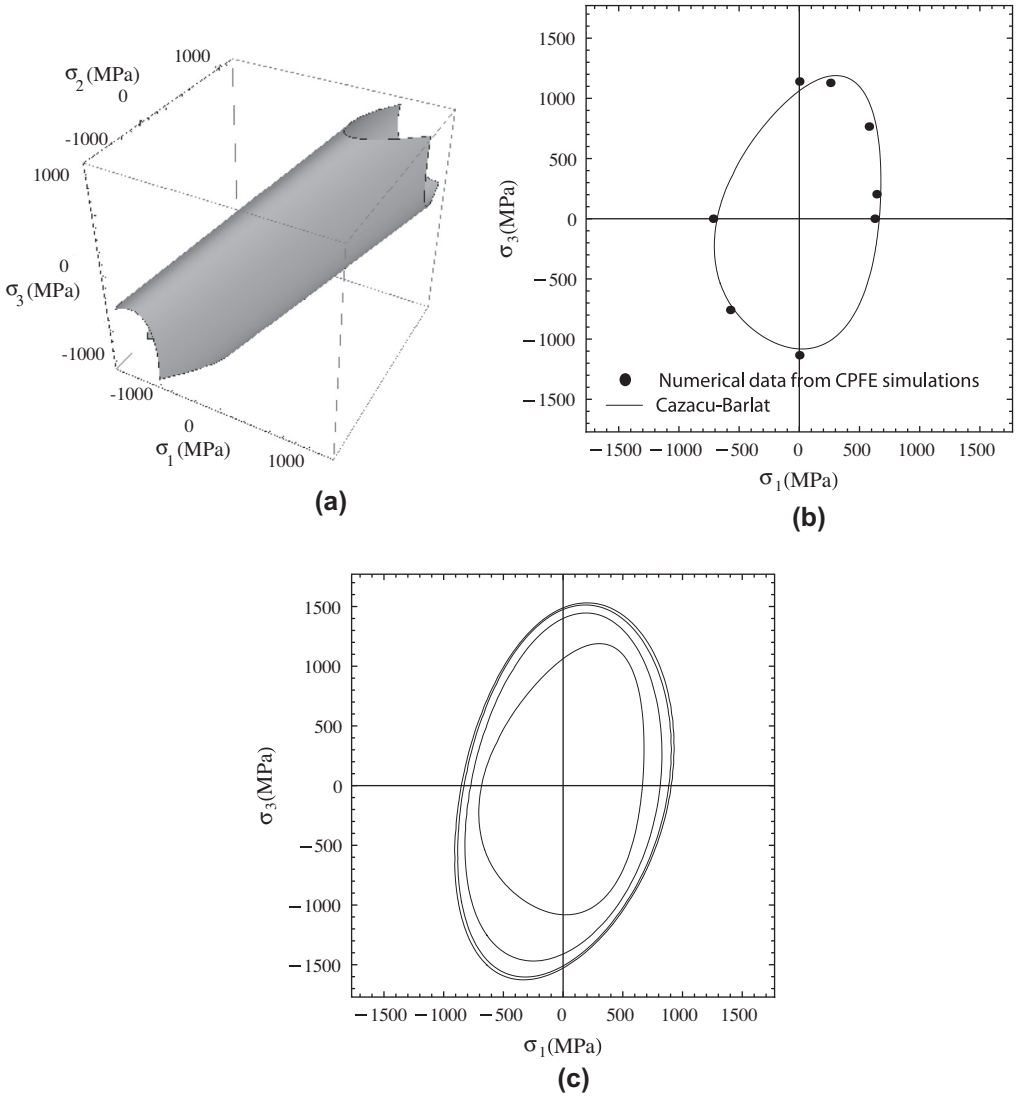

Fig. 9. Yield loci for the microstructural RVE M10: (a) 3D yield locus at $W_p = 0.1$ MPa, (b) $\sigma_1 - \sigma_3$ yield locus at $W_p = 0.1$ MPa, compared with the numerical data obtained from CPFE simulations, and (c) evolution of the yield locus with plastic work increase corresponding to $W_p = 0.1$, 1.0, 4.0 and 10.0 MPa.

Table 5
Calibrated values of anisotropic parameters of Eq. (20), corresponding to $W_p = 0.1$ MPa for microstructure M10.

a_1	a_2	a_3	a_4	a_5	a_6	b_1	b_2	b_3	b_4
0.364	0.060	0.108	1	0.542	0.547	−0.048	0.026	−0.072	0.023

are smaller than those of a_i. This is observed in other microstructures as well. Consequently, some of the b_i parameters in the *C–B* yield criterion are set to zero to reduce the number of coefficients that requires calibration.

In the first iteration, all b_i parameters are set to zero. This reduces the *C–B* criterion to the Hill's model with only 6 anisotropic parameters. The process of calibrating the anisotropic parameters is repeated by least square minimization of this function:

$$\min_{a_i(i=1,..,6)} \sum_{I=1}^{19} [(J_2^0)_I^{3/2} - Y_f^3]^2 \tag{21}$$

where $(J_2^0)_I$ is obtained from Eq. (18). The calibrated parameters in the Hill's model, corresponding to $W_p = 0.1$ MPa, are summarized in Table 6. The resulting Hill's yield surface at $W_p = 0.1$ MPa, projected on the $\sigma_1 - \sigma_3$ plane, is shown in Fig. 10(a). Comparing this yield locus with the *C–B* yield locus in Fig. 10(a) shows reasonable difference.

In the second iteration, the parameters b_i $(i = 5, 6, \ldots, 11)$ are set to zero. This removes the shear terms from J_3^0, and the number of parameters, which require calibration, reduces to 10. In this case only 15 loading conditions are considered for homogenization and calibration purposes, which are:

- Three uniaxial tension tests in the x, y and z directions.
- Three pure shear tests in xy, xz and yz planes.
- Three uniaxial compression tests in the x, y and z directions.
- Three biaxial tension tests ($\epsilon_{xx} : \epsilon_{yy} = 1 : 1$ with $\sigma_{zz} = 0$; $\epsilon_{zz} : \epsilon_{xx} = 1 : 1$ with $\sigma_{yy} = 0$; and $\epsilon_{yy} : \epsilon_{zz} = 1 : 1$ with $\sigma_{xx} = 0$).
- Three biaxial compression tests ($\epsilon_{xx} : \epsilon_{yy} = -1 : -1$ with $\sigma_{zz} = 0$; $\epsilon_{zz} : \epsilon_{xx} = -1 : -1$ with $\sigma_{yy} = 0$; and $\epsilon_{yy} : \epsilon_{zz} = -1 : -1$ with $\sigma_{xx} = 0$).

The parameters a_i $(i = 1, \ldots, 6)$ and b_i $(i = 1, \ldots, 4)$ are calibrated by least square minimization of this function:

$$\min_{a_i(i=1,..,6),b_i(i=1,...,4)} \sum_{I=1}^{15} [(J_2^0)_I^{3/2} - (J_3^*)_I - Y_f^3]^2 \tag{22}$$

where $(J_3^*)_I$ is the reduced form of $(J_3^0)_I$ as:

$$\begin{aligned}(J_3^*)_I = {} & \frac{1}{27}(b_1+b_2)(\sigma_{xx}^I)^3 + \frac{1}{27}(b_3+b_4)(\sigma_{yy}^I)^3 + \frac{1}{27}[2(b_1+b_4)-(b_2+b_3)](\sigma_{zz}^I)^3 + \frac{2}{9}(b_1+b_4)\sigma_{xx}^I\sigma_{yy}^I\sigma_{zz}^I \\ & - \frac{1}{9}(b_1\sigma_{yy}^I + b_2\sigma_{zz}^I)(\sigma_{xx}^I)^2 - \frac{1}{9}(b_3\sigma_{zz}^I + b_4\sigma_{xx}^I)(\sigma_{yy}^I)^2 - \frac{1}{9}[(b_1-b_2+b_4)\sigma_{xx}^I + (b_1-b_3+b_4)\sigma_{yy}^I](\sigma_{zz}^I)^2\end{aligned} \tag{23}$$

It should be noted that the reduced *C–B* criterion, $(J_2^0)^{\frac{3}{2}} - J_3^* - Y_f^3 = 0$, still satisfies the required characteristics for an acceptable yield criterion, viz. pressure-insensitivity, anisotropy and tension–compression asymmetry. The calibrated parameters corresponding to $W_p = 0.1$ MPa are summarized in Table 7. The resulting yield surface at $W_p = 0.1$ MPa, projected on the $\sigma_1 - \sigma_3$ plane, is shown in Fig. 10(b). This yield locus, when compared with the one obtained from *C–B* model with all 17 parameters shows no significant difference. Thus the *C–B* yield model with reduced number of parameters will be used to develop the macroscopic HAPC constitutive model for Ti alloys.

4.3. Evaluation of microstructure dependent constitutive parameters in the HAPC model

The anisotropic parameters a_i $(i = 1, \ldots, 6)$, b_i $(i = 1, \ldots, 4)$ and the flow stress (Y_f) in the reduced *C–B* model are microstructure-dependent. To adequately account for microstructural variations, 70 different polycrystalline RVEs with different microstructure descriptors are considered. The characteristics of these microstructures are summarized in Table 8 in Appendix A. Each RVE consists of $7 \times 7 \times 7$ cubic grains. The volume averages of Schmid factors $\overline{SF}_x, \overline{SF}_y$ and $\overline{SF}_z$ vary between 0.146 and 0.498 in the microstructures. Three values, viz. 7.5, 15 and 40 μm are considered for the average grain size D.

For each RVE, CPFE simulations are conducted under 12 different loading conditions, viz.:

Table 6
Calibrated values of Hill's anisotropic parameters, corresponding to $W_p = 0.1$ MPa for microstructure M10.

a_1	a_2	a_3	a_4	a_5	a_6
0.359	0.055	0.105	1	0.542	0.547

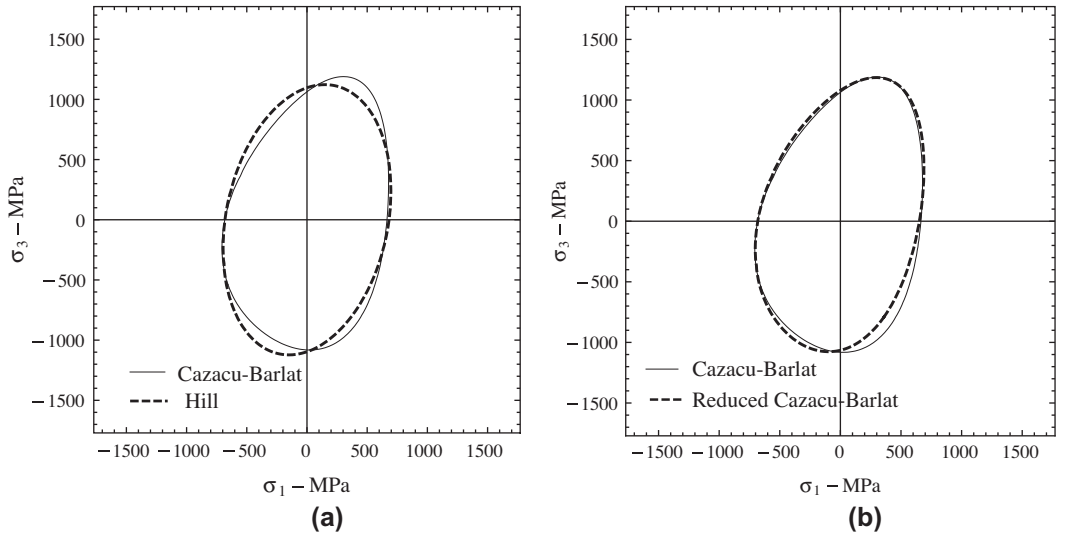

Fig. 10. $\sigma_1 - \sigma_3$ yield loci for microstructure M10, corresponding to $W_p = 0.1$ MPa. (a) Comparison of the Cazacu–Barlat model with 17 parameters with Hill's anisotropic model and (b) comparison of the 17 and 10 (reduced) parameter *C–B* models.

Table 7
Calibrated values of the reduced Cazacu–Barlat parameters at $W_p = 0.1$ MPa for the microstructure M10.

a_1	a_2	a_3	a_4	a_5	a_6	b_1	b_2	b_3	b_4
0.359	0.074	0.093	1	0.542	0.547	−0.032	−0.004	−0.057	0.003

- Three uniaxial tension tests in the x, y and z directions.
- Three pure shear tests in xy, xz and yz planes.
- Three uniaxial compression tests in the x, y and z directions.
- Three biaxial tension tests ($\epsilon_{xx} : \epsilon_{yy} = 1 : 1$ with $\sigma_{zz} = 0$; $\epsilon_{zz} : \epsilon_{xx} = 1 : 1$ with $\sigma_{yy} = 0$; and $\epsilon_{yy} : \epsilon_{zz} = 1 : 1$ with $\sigma_{xx} = 0$).

For each microstructure, the flow stress Y_f is obtained at different values of W_p and the anisotropic parameters for each microstructure are evaluated at different values of W_p by least square minimization of the function:

$$\min_{a_i(i=1,\ldots,6),b_i(i=1,\ldots,4)} \sum_{I=1}^{12} [(J_2^0)_I^{3/2} - (J_3^*)_I - Y_f^3]^2 \tag{24}$$

The procedure in Section 4.2.1 is used to calibrate a_i ($i = 1, \ldots, 6$) and b_i ($i = 1, \ldots, 4$). A few key observations are made from the homogenization studies.

- Anisotropic yield parameters for each microstructure evolves with averaged plastic work W_p.
- The flow stress for each microstructure evolves with increase in plastic work W_p.
- The flow stress for a given value of W_p decreases with increase in the average grain size, D.
- If $\overline{SF}_i > \overline{SF}_j > \overline{SF}_k$ then $a_l > a_m > a_n$, where a_l, a_m, a_n are the anisotropic parameters associated with the normal stress components in the J_2^0 part of the yield criterion, i.e.

$$J_2^0 = \frac{a_l}{6}(\sigma_i - \sigma_j)^2 + \frac{a_m}{6}(\sigma_i - \sigma_k)^2 + \frac{a_n}{6}(\sigma_j - \sigma_k)^2 + a_4\sigma_{xy}^2 + a_5\sigma_{xz}^2 + a_6\sigma_{yz}^2 \tag{25}$$

- Higher Schmid factors in x and y directions result in lower flow stress Y_f.

The calibrated values of the anisotropic parameters a_i and b_i and the flow stress Y_f for different RVEs are used to derive a functional forms of parameters in the HAPC model in terms of microstructural descriptor statistics $\overline{SF}_x$, $\overline{SF}_y$, $\overline{SF}_z$ and D, as well as the evolving plastic work W_p. Power law functional forms are assumed for the parameters as:

$$a_i = (A_1^i + A_2^i \overline{SF}_x^{\alpha_i})(A_3^i + A_4^i \overline{SF}_y^{\beta_i})(A_5^i + A_6^i \overline{SF}_z^{\gamma_i})(A_7^i + A_8^i D^{\eta_i})(A_9^i + A_{10}^i W_p^{\kappa_i}) \quad i = 1, \ldots, 6$$

$$b_i = (B_1^i + B_2^i \overline{SF}_x^{\chi_i})(B_3^i + B_4^i \overline{SF}_y^{\delta_i})(B_5^i + B_6^i \overline{SF}_z^{\epsilon_i})(B_7^i + B_8^i D^{\phi_i})(B_9^i + B_{10}^i W_p^{\varphi_i}) \quad i = 1, \ldots, 4$$

$$Y_f = (C_1^i + C_2^i \overline{SF}_x^{\lambda})(C_3^i + C_4^i \overline{SF}_y^{\mu})(C_5^i + C_6^i \overline{SF}_z^{\nu})(C_7^i + C_8^i D^{\theta})(C_9^i + C_{10}^i W_p^{\psi}) \tag{26}$$

The coefficients $A_j^i, B_j^i, C_i, \beta_i, \gamma_i, \eta_i, \kappa_i, \chi_i, \delta_i, \epsilon_i, \phi_i, \varphi_i, \lambda, \mu, \nu, \theta$ and ψ are obtained from a least square fit of the data for RVEs in Table 8. The resulting values of the coefficients are given in Tables 9–12 in Appendix B. The strength of the dependencies are generally indicated by the exponents. For example, a weak dependence is signaled by a near-zero exponent. The corresponding values of a_i, b_i and Y_f are given below.

$$a_1 = (0.9 + 15.6\overline{SF}_x^{1.9})(0.3 + 5.9\overline{SF}_y^{1.8})(0.01 - 6.6\overline{SF}_z^{10.6})(-66.6 - 0.4D^{0.5})(-2.2 + 2.3W_p^{0.002})$$

$$a_2 = (1.6 + 14.2\overline{SF}_x^{2.1})(0.4 - 1.1\overline{SF}_y^{2.2})(0.04 + 2.4\overline{SF}_z^{2.5})(-40.0 - 0.1D^{0.4})(0.8 - 0.8W_p^{0.003})$$

$$a_3 = (1.6 - 3.2\overline{SF}_x^{1.8})(0.4 + 4.7\overline{SF}_y^{2.6})(0.08 + 4.8\overline{SF}_z^{2.0})(33.8 + 0.03D^{0.8})(-1.2 + 1.2W_p^{0.001})$$

$$a_4 = 1.0$$

$$a_5 = (0.2 + 3.4\overline{SF}_x^{-0.01})(0.05 - 0.07\overline{SF}_y^{1.4})(0.05 + 0.2\overline{SF}_z^{1.9})(36.4 - 1.3D^{0.1})(-3.0 + 6 \times 10^{-7} W_p^{4.5})$$

$$a_6 = (-3.9 + 4.2\overline{SF}_x^{-0.1})(-0.1 + 0.8\overline{SF}_y^{7.8})(0.2 + 0.9\overline{SF}_z^{1.1})(-5.2 + 0.002D^{1.0})(6.1 - 0.006W_p^{0.7})$$

$$b_1 = -5.4(0.01 + 0.6\overline{SF}_x^{3.4})(0.5 + 0.1\overline{SF}_y^{2.8})\overline{SF}_z^{3.7}(22.1 + 0.1D^{0.8})(0.2 + 0.3W_p^{0.3})$$

$$b_2 = (1.6 - 1.8\overline{SF}_x^{0.1})(1.5 - 2.1\overline{SF}_y^{0.7})(1.6 - 2.6\overline{SF}_z^{1.1})(42.6 + 0.3D^{0.8})(-2.0 + 2.0W_p^{0.01})$$

$$b_3 = (0.8 + 2.4\overline{SF}_x^{2.7})(-0.8 + 5.7\overline{SF}_y^{1.7})(-0.002 - 0.03\overline{SF}_z^{3.8})(24.7 + 0.1D^{1.0})(0.2 + 1.0W_p^{0.2})$$

$$b_4 = (1.8 - 2.0\overline{SF}_x^{0.2})(1.8 - 2.0\overline{SF}_y^{0.6})(1.9 - 3.6\overline{SF}_z^{1.9})(34.5 + 0.1D^{1.0})(1.4 - 1.4W_p^{0.003})$$

$$Y_f = (3.7 - 39.1\overline{SF}_x^{7.6})(0.7 - 40.4\overline{SF}_y^{9.8})(16.2 + 17.7\overline{SF}_z^{1.0})(40.5 - 12.9D^{0.1})(-3.3 + 3.5W_p^{0.005}) \tag{27}$$

It is clear from these expressions that the macroscopic constitutive parameters and consequently the yield function not only depend on morphological and crystallographic features of the polycrystalline microstructure, but also on the evolution of internal variables during the deformation process.

4.4. An extension of the homogenized model to account for rate dependency

A rate-dependent viscoplastic extension of the HAPC model is proposed in this section. The rate-dependent framework follows an over-stress viscoplastic model (Perzyna, 1966) with anisotropy introduced through the yield functions developed in Section 4.3. In this model, the viscoplastic strain rate is expressed in terms of a function $\phi(F)$ of the overstress F as:

$$\dot{\boldsymbol{\epsilon}}^p = \lambda_0 \phi(F) \frac{\partial F/\partial \boldsymbol{\sigma}}{\|\partial F/\partial \boldsymbol{\sigma}\|} \tag{28}$$

where λ_0 is a temperature dependent viscosity coefficient. The viscoplastic strain rate in Eq. (28) follows the associated flow rule and hence satisfies normality and incompressibility conditions. In Perzyna (1966) and Ghosh and Kikuchi (1991) a power law expression, i.e. $\phi(F) = \langle F \rangle^n$ has been discussed to adequately represent the behavior of most metals. $\langle\ \rangle$ is the McCauley operator corresponding to the positive sign of the argument. The over-stress F corresponds to a measure of the excess equivalent flow stress σ_{eq} over the rate-independent yield stress Y_f, i.e.

$$F = \sigma_{eq} - Y_f \tag{29}$$

where

$$\begin{aligned}\sigma_{eq}^3 = (J_2^0)^{3/2} - J_3^* = &\left[\frac{a_1}{6}(\sigma_{xx} - \sigma_{yy})^2 + \sigma_{xy}^2 + a_5\sigma_{xz}^2 + a_6\sigma_{yz}^2\right]^{\frac{3}{2}} \\ &- \left[\frac{1}{27}(b_1 + b_2)\sigma_{xx}^3 + \frac{1}{27}b_3\sigma_{yy}^3 + \frac{1}{27}[2b_1 - (b_2 + b_3)]\sigma_{zz}^3 + \frac{2}{9}b_1\sigma_{xx}\sigma_{yy}\sigma_{zz} - \frac{1}{9}(b_1\sigma_{yy} + b_2\sigma_{zz})\sigma_{xx}^2\right. \\ &\left. - \frac{1}{9}b_3\sigma_{zz}\sigma_{yy}^2 - \frac{1}{9}[(b_1 - b_2)\sigma_{xx} + (b_1 - b_3)\sigma_{yy}]\sigma_{zz}^2\right]\end{aligned} \tag{30}$$

The anisotropy parameters a_i and b_i, as well as the rate-independent yield stress Y_f in Eq. (29) are given in Eqs. (27). These parameters evolve with plastic work.

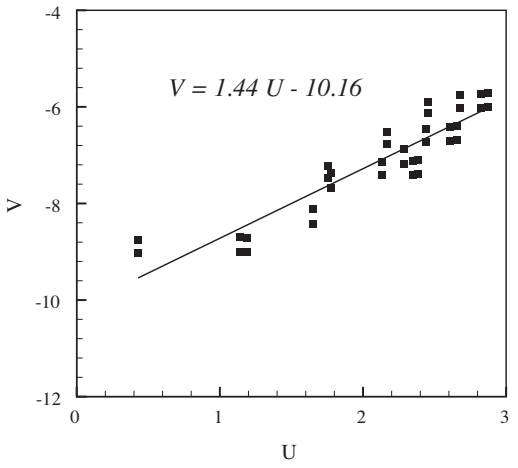

Fig. 11. Calibration of viscoplastic parameters λ_0 and n.

The homogenized viscosity coefficient λ_0 and exponent n in Eq. (28) are calibrated from a set of loading conditions combining N different imposed *strain ratios* and M different applied *strain-rates*. In each increment, the stress tensor $\boldsymbol{\sigma}$, the plastic strain rate tensor $\dot{\boldsymbol{\epsilon}}^p$, and the plastic work W_p are computed from CPFE simulation results. The corresponding yield stress $Y_f(W_p)$ and anisotropy coefficients a_i and b_i are evaluated using Eqs. (27). The overstress F is obtained at each time increment from Eqs. (29) and (30) and its derivative with respect to σ_{ij} is evaluated as:

$$\frac{\partial F}{\partial \sigma_{ij}} = \frac{\partial \sigma_{eq}}{\partial \sigma_{ij}} = \frac{1}{3}[(J_2^0)^{3/2} - J_3^*]^{-2/3}\left[\frac{3}{2}(J_2^0)^{1/2}\frac{\partial J_2^0}{\partial \sigma_{ij}} - \frac{\partial J_3^*}{\partial \sigma_{ij}}\right] \tag{31}$$

To determine λ_0 and n, Eq. (28) is rewritten by taking the logarithm of both sides as:

$$\ln(\dot{\epsilon}_{ij}^p) = \ln(\lambda_0) + n\ln\langle F\rangle + \ln\left(\frac{\partial F/\partial \sigma_{ij}}{\|\partial F/\partial \boldsymbol{\sigma}\|}\right)$$

or

$$\ln\left[\frac{\dot{\epsilon}_{ij}^p \|\partial F/\partial \boldsymbol{\sigma}\|}{\partial F/\partial \sigma_{ij}}\right] = \ln(\lambda_0) + n\ln\langle F\rangle \tag{32}$$

Eq. (32) is a linear relation between $U(=\ln\langle F\rangle)$ and $V(=\ln\left[\frac{\dot{\epsilon}_{ij}^p\|\partial F/\partial \boldsymbol{\sigma}\|}{\partial F/\partial \sigma_{ij}}\right])$. Consequently, a plot of V versus U yields a straight line with slope equal to n and the intercept equal to $\ln(\lambda_0)$. The viscoplastic parameters λ_0 and n are consequently obtained by finding the best linear fit to the measured data (U, V) corresponding to different stress components for different loading conditions at different time increments. Four different strain rates under uniaxial tension are applied to calibrate these parameters, corresponding to $N = 1$ and $M = 4$. The applied strain rates are: $\dot{\epsilon}_{xx}^{(1)} = 0.0001\ \mathrm{s}^{-1}$, $\dot{\epsilon}_{xx}^{(2)} = 0.0005\ \mathrm{s}^{-1}$, $\dot{\epsilon}_{xx}^{(3)} = 0.001\ \mathrm{s}^{-1}$ and $\dot{\epsilon}_{xx}^{(4)} = 0.002\ \mathrm{s}^{-1}$. Fig. 11 shows the best linear fit to the measured data at different time increments considering only $\dot{\epsilon}_{xx}^p$ and $\dot{\epsilon}_{yy}^p$. The corresponding viscoplastic parameters are evaluated as:

$$\lambda_0 = e^{-10.16} = 3.9 \times 10^{-5} \quad \text{and} \quad n = 1.44 \tag{33}$$

The methodology discussed in this section provides a path for extending the rate-independent continuum anisotropic plasticity model derived from homogenization of polycrystalline crystal plasticity finite element simulation results into a rate-dependent model. The utilization of this model will be provided in a future paper.

5. Conclusion

The first part of this two part paper is aimed at developing a homogenized, anisotropic plasticity constitutive (HAPC) model for Ti alloys. In particular, this model develops an anisotropic yield function with a direct connection to the morphology and crystalline structure of the polycrystalline microstructure that can be incorporated in any macroscopic FEM code. The advantage of this model is that it avoids having to perform computationally expensive micromechanical analysis at each point in macroscopic simulations. It is able to capture important deformation characteristics of Ti-based alloys, which are pressure insensitivity, anisotropy and tension–compression asymmetry. The overall framework of the HAPC model follows

Table 8
Microstructure descriptors for different RVEs used to develop the HAPC model.

RVE	$\overline{SF}_x$	$\overline{SF}_y$	$\overline{SF}_z$	D	RVE	$\overline{SF}_x$	$\overline{SF}_y$	$\overline{SF}_z$	D
M10	0.471	0.47	0.146	7.5	M130	0.437	0.268	0.47	7.5
M11	0.471	0.47	0.146	15	M131	0.437	0.268	0.47	15
M12	0.471	0.47	0.146	40	M132	0.437	0.268	0.47	40
M20	0.445	0.446	0.36	7.5	M140	0.47	0.473	0.428	7.5
M21	0.445	0.446	0.36	15	M141	0.47	0.473	0.428	15
M22	0.445	0.446	0.36	40	M142	0.47	0.473	0.428	40
M30	0.445	0.446	0.496	7.5	M150	0.323	0.448	0.382	7.5
M31	0.445	0.446	0.496	15	M151	0.323	0.448	0.382	15
M32	0.445	0.446	0.496	40	M152	0.323	0.448	0.382	40
M40	0.43	0.435	0.401	7.5	M160	0.482	0.498	0.483	7.5
M41	0.43	0.435	0.401	15	M161	0.482	0.498	0.483	15
M42	0.43	0.435	0.401	40	M162	0.482	0.498	0.483	40
M50	0.47	0.437	0.268	7.5	M171	0.146	0.471	0.47	15
M51	0.47	0.437	0.268	15	M172	0.146	0.471	0.47	40
M52	0.47	0.437	0.268	40	M180	0.36	0.445	0.446	7.5
M60	0.428	0.47	0.473	7.5	M181	0.36	0.445	0.446	15
M61	0.428	0.47	0.473	15	M182	0.36	0.445	0.446	40
M62	0.428	0.47	0.473	40	M190	0.496	0.445	0.446	7.5
M70	0.382	0.323	0.448	7.5	M191	0.496	0.445	0.446	15
M71	0.382	0.323	0.448	15	M192	0.496	0.445	0.446	40
M72	0.382	0.323	0.448	40	M200	0.401	0.43	0.435	7.5
M80	0.483	0.482	0.498	7.5	M201	0.401	0.43	0.435	15
M81	0.483	0.482	0.498	15	M202	0.401	0.43	0.435	40
M82	0.483	0.482	0.498	40	M210	0.268	0.47	0.437	7.5
M91	0.47	0.146	0.471	15	M211	0.268	0.47	0.437	15
M92	0.47	0.146	0.471	40	M212	0.268	0.47	0.437	40
M100	0.446	0.36	0.445	7.5	M220	0.473	0.428	0.47	7.5
M101	0.446	0.36	0.445	15	M221	0.473	0.428	0.47	15
M102	0.446	0.36	0.445	40	M222	0.473	0.428	0.47	40
M110	0.446	0.496	0.445	7.5	M230	0.448	0.382	0.323	7.5
M111	0.446	0.496	0.445	15	M231	0.448	0.382	0.323	15
M112	0.446	0.496	0.445	40	M232	0.448	0.382	0.323	40
M120	0.435	0.401	0.43	7.5	M240	0.498	0.483	0.482	7.5
M121	0.435	0.401	0.43	15	M241	0.498	0.483	0.482	15
M122	0.435	0.401	0.43	40	M242	0.498	0.483	0.482	40

Table 9
Coefficients A_j^i in Eq. (27).

i/j	$j=1$	$j=2$	$j=3$	$j=4$	$j=5$	$j=6$	$j=7$	$j=8$	$j=9$	$j=10$
$i=1$	0.9	15.6	0.3	5.9	0.01	−6.6	66.6	0.4	−2.19	2.25
$i=2$	1.6	14.2	0.4	1.1	0.04	2.4	40.0	0.1	0.79	−0.82
$i=3$	1.6	−3.2	0.4	4.7	0.08	4.8	33.8	0.03	−1.21	1.22
$i=4$	1.0	0.0	1.0	0.0	1.0	0.0	1.0	0.0	1.0	0.0
$i=5$	0.2	3.4	0.05	−0.07	0.05	0.2	36.4	1.3	−3.04	6×10^{-7}
$i=6$	3.9	4.2	−0.1	0.8	0.2	0.9	−5.2	0.002	6.06	−0.006

Table 10
Coefficients B_j^i in Eq. (27).

i/j	$j=1$	$j=2$	$j=3$	$j=4$	$j=5$	$j=6$	$j=7$	$j=8$	$j=9$	$j=10$
$i=1$	0.01	0.6	0.5	0.1	2×10^{-4}	5.4	22.1	0.1	0.15	0.29
$i=2$	1.6	−1.8	1.5	−2.1	1.6	−2.6	42.6	0.3	−1.97	2.02
$i=3$	0.8	2.4	−0.8	5.7	0.002	0.03	24.7	0.1	0.23	0.95
$i=4$	1.8	2.0	1.8	−2.0	1.9	−3.6	34.5	0.1	1.42	−1.44

Table 11
Coefficients C_j^i in Eq. (27).

i/j	$j=1$	$j=2$	$j=3$	$j=4$	$j=5$	$j=6$	$j=7$	$j=8$	$j=9$	$j=10$
$i=1$	3.7	39.1	0.7	−40.4	16.2	17.7	40.5	−12.9	−3.3	3.5

Table 12
Various coefficients in Eq. (27).

	α_i	β_i	γ_i	η_i	κ_i	χ_i	δ_i	ϵ_i	ϕ_i	φ_i	λ	μ	ν	θ	ψ
$i=1$	1.9	1.8	10.6	0.5	0.002	3.4	2.8	3.7	0.8	0.3	7.6	9.8	1.0	0.1	0.005
$i=2$	2.1	2.2	2.5	0.4	0.003	0.1	0.7	1.1	0.8	0.01					
$i=3$	1.8	2.6	2.0	0.8	0.001	2.7	1.7	3.8	1.0	0.2					
$i=4$	–	–	–	–	–	0.2	0.6	1.9	1.0	0.03					
$i=5$	−0.01	1.4	1.9	0.1	4.5										
$i=6$	−0.1	7.8	1.1	1.0	0.7										

the structure of the anisotropic Cazacu–Barlat yield function that possesses the desired attributes of anisotropy and tension–compression asymmetry inherent to polycrystalline metals. This framework is further extended to accommodate rate-dependent behavior observed in mechanical behavior of Ti alloys. Parameters in the HAPC model are calibrated from results of homogenization of microstructural CPFEM analysis variables of the polycrystalline RVEs with varying orientation distributions and grain sizes.

A systematic sensitivity analysis is conducted to establish the dependence of mechanical response on microstructural crystallographic and morphological parameters. This analysis concludes that average Schmid factors for three orthogonal directions and grain size distributions are important microstructural descriptors that should be incorporated in the homogenized yield functions. Parameters in the anisotropic yield function following the Cazacu–Barlat framework are calibrated from homogenization of CPFE results of polycrystalline microstructure simulations. The anisotropy parameters in the homogenized yield function are found to be functions of the microstructural descriptors, but evolve with plastic work. The functional forms of the parameters overcome limitations of constant anisotropy parameters that are conventionally assumed in anisotropic plasticity models. Comparison of the anisotropic HAPC model results with homogenized micromechanics results shows excellent agreement. The HAPC model has a significant efficiency advantage over the micromechanics models and is hence a very effective tool in making macroscopic deformation predictions with explicit reference to the microstructural composition. The second part of this two-part paper develops a probabilistic crack nucleation model for structural scale analysis of polycrystalline Ti alloys from grain-level crack nucleation results.

Acknowledgments

This work has been supported by the Air Force Office of Scientific through a Discovery Challenge Grant (DCT Grant # FA-9550-09-1-0452, Program Manager: Dr. David Stargel). This sponsorship is gratefully acknowledged.

Appendix A

See Table 8.

Appendix B

See Tables 9–12.

References

Acharya, A., Beaudoin, A.J., 2000. Grain-size effect in viscoplastic polycrystals at moderate strains. J. Mech. Phys. Solids 48, 2213–2230.
An, Y., Vegter, H., Carless, L., Lambriks, M., 2011. A novel yield locus description by combining the Taylor and the relaxed Taylor theory for sheet steels. Int. J. Plast. 27 (11), 1758–1780.
Anahid, M., Samal, M.K., Ghosh, S., 2011. Dwell fatigue crack nucleation model based on crystal plasticity finite element simulations of polycrystalline Titanium alloys. J. Mech. Phys. Solids 59 (10), 2157–2176.
Anand, L., Kothari, M., 1996. A computational procedure for rate-independent crystal plasticity. J. Mech. Phys. Solids 44, 525–558.
Ashby, M.F., 1970. The deformation of plastically non-homogeneous materials. Philos. Mag. 21, 399–424.
Bache, M.R., 2003. A review of dwell sensitive fatigue in titanium alloys: the role of microstructure texture and operating conditions. Int. J. Fatigue 25, 1079–1087.
Balasubramanian, S., Anand, L., 1996. Single crystal and polycrystal elastoviscoplasticity: application to earing in cup drawing of fcc materials. Comput. Mech. 17, 209–225.
Barbe, F., Decker, L., Jeulin, D., Cailletaud, G., 2001a. Intergranular and intragranular behavior of polycrystalline aggregates. Part 1: F.E. model. Int. J. Plast. 17 (4), 513–536.
Barbe, F., Forest, S., Cailletaud, G., 2001b. Intergranular and intragranular behavior of polycrystalline aggregates. Part 2: results. Int. J. Plast. 17 (4), 537–563.
Bohlke, T., Risy, G., Bertram, A., 2006. Finite element simulation of metal forming operations with texture based material models. Model. Simul. Mater. Sci. Eng. 14, 365–387.
Bridiera, F., McDowell, D.L., Villechaisea, P., Mendeza, J., 2009. Crystal plasticity modeling of slip activity in Ti-6Al-4V under high cycle fatigue loading. Int. J. Plast. 25, 1066–1082.
Cazacu, O., Barlat, F., 2001. Generalization of Druckers yield criterion to orthotropy. Math. Mech. Solids 6, 613–630.
Cazacu, O., Barlat, F., 2003. Application of representation theory to describe yielding of anisotropic aluminum alloys. Int. J. Eng. Sci. 41, 13671385.
Cazacu, O., Barlat, F., 2004. A criterion for description of anisotropy and yield differential effects in pressure-insensitive metals. Int. J. Plast. 20, 2027–2045.

Deka, D., Joseph, D.S., Ghosh, S., Mills, M.J., 2006. Crystal plasticity modeling of deformation and creep in polycrystalline Ti-6242. Metall. Trans. A. 37A (5), 1371–1388.
Fan, X.G., Yang, H., 2011. Internal-state-variable based self-consistent modeling for hot working of two-phase titanium alloys coupling microstructure evolution. Int. J. Plast. 27, 1833–1852.
Feyel, F., Chaboche, J., 2000. FE2 multiscale approach for modelling the elastoviscoplastic behaviour of long fiber SiC/Ti composite materials. Comput. Meth. Appl. Mech. Eng. 183, 309–330.
Ghosh, S., Bai, J., Paquet, D., 2009. Homogenization-based continuum plasticity-damage model for ductile failure of materials containing heterogeneities. J. Mech. Phys. Solids 57, 1017–1044.
Ghosh, S., Bhandari, Y., Groeber, M., 2008. CAD based reconstruction of three dimensional polycrystalline microstructures from FIB generated serial sections. J. Comput.-Aided Des. 40 (3), 293–310.
Ghosh, S., Kikuchi, N., 1991. An arbitrary LagrangianEulerian finite element method for large deformation analysis of elastic–viscoplastic solids. Comput. Meth. Appl. Mech. Eng. 86, 127–188.
Ghosh, S., Lee, K., Raghavan, P., 2001. A multi-level computational model for multi-scale damage analysis in composite and porous materials. Int. J. Solids Struct. 38, 2335–2385.
Goh, C.H., Neu, R.W., McDowell, D.L., 2003. Crystallographic plasticity in fretting of Ti-6AL-4V. Int. J. Plast. 19, 1627–1650.
Groeber, M., Ghosh, S., Uchic, M.D., Dimiduk, D.M., 2008a. A framework for automated analysis and representation of 3D polycrystalline microstructures, part 1: statistical characterization. Acta Mater. 56 (6), 1257–1273.
Groeber, M., Ghosh, S., Uchic, M.D., Dimiduk, D.M., 2008b. A framework for automated analysis and representation of 3D polycrystalline microstructures, part 2: synthetic structure generation. Acta Mater. 56 (6), 1274–1287.
Hasija, V., Ghosh, S., Mills, M.J., Joseph, D.S., 2003. Modeling deformation and creep in Ti-6Al alloys with experimental validation. Acta Mater. 51, 4533–4549.
Hill, R., 1948. A theory of the yielding and plastic flow of anisotropic metals. Proc. R. Soc. London Ser. A 193, 281–297.
Hosford, W.F., 1966. Texture strengthening. Met. Eng. Q. 6, 13–19.
Imam, M.A., Gilmore, C.M., 1979. Room temperature creep of Ti-6Al-4V. Metall. Trans. A 10A, 419–425.
Inal, K., Mishra, R.K., Cazacu, O., 2010. Forming simulation of aluminum sheets using an anisotropic yield function coupled with crystal plasticity theory. Int. J. Solids Struct. 47, 2223–2233.
Jain, J.R., Ghosh, S., 2008. A 3D continuum damage mechanics model from micromechanical analysis of fiber reinforced composites with interfacial damage. ASME J. Appl. Mech. 75 (3), 031011-1–031011-15.
Khan, A.S., Kazmi, R., Farrokh, B., 2007. Multiaxial and non-proportional loading responses, anisotropy and modeling of Ti-6Al-4V titanium alloy over wide ranges of strain rates and temperatures. Int. J. Plast. 23 (6), 931–950.
Khan, A.S., Suh, Y.S., Kazmi, R., 2004. Quasi-static and dynamic loading responses and constitutive modeling of titanium alloys. Int. J. Plast. 20 (12), 2233–2248.
Khan, A.S., Yu, S., Liu, H., 2012. Deformation induced anisotropic responses of Ti-6Al-4V alloy. Part II: a strain rate and temperature dependent anisotropic yield criterion. Int. J. Plast. 28, 14–26.
Kouznetsova, V., Brekelmans, W., Baaijens, F., 2001. An approach to micro-macro modeling of hetergeneous materials. Comput. Mech. 27, 37–48.
McDowell, D.L., Dunne, F.P.E., 2010. Microstructure-sensitive computational modeling of fatigue crack formation. Int. J. Fatigue 32, 1521–1542.
Miller, R.M., Bieler, T.R., Semiatin, S.L., 1999. Flow softening during hot working of Ti-6Al-4V with a lamellar colony microstructure. Scripta Mater. 40 (12), 1387–1393.
Morrissey, R., Goh, C.H., McDowell, D.L., 2003. Microstructure-scale modeling of HCF deformation. Mech. Mater. 35, 295–311.
Neeraj, T., Hou, D.H., Daehn, G.S., Mills, M.J., 2000. Phenomenological and microstructural analysis of room temperature creep in Titanium alloys. Acta Mater. 48, 1225–1238.
Nixon, M.E., Cazacu, O., Lebensohn, R.A., 2010. Anisotropic response of high-purity α-titanium: experimental characterization and constitutive modeling. Int. J. Plast. 26, 516–532.
Nye, J.F., 1953. Some geometrical relations in dislocated crystals. Acta Metall. 1, 153–162.
Paquet, P., Dondeti, P., Ghosh, S., 2011. Dual-stage nested homogenization for rate-dependent anisotropic elasto-plasticity model of dendritic cast aluminum alloys. Int. J. Plast. 27 (10), 1677–1701.
Perzyna, P., 1966. Fundamental problems in viscoplasticity. Adv. Appl. Mech. 9, 243–377.
Raabe, D., Roters, F., 2004. Using texture components in crystal plasticity finite element simulations. Int. J. Plast. 20, 339–361.
Raabe, D., Zhao, Z., Roters, F., 2004. Study on the orientational stability of cube-oriented FCC crystals under plane strain by use of a texture component crystal plasticity finite element method. Scripta Mater. 50, 1085–1090.
Rossiter, J., Brahme, A., Simha, M.H., Inal, K., Mishra, R., 2010. A new crystal plasticity scheme for explicit time integration codes to simulate deformation in 3D microstructures: effects of strain path strain rate and thermal softening on localized deformation in the aluminum alloy 5754 during simple shear. Int. J. Plast. 26 (12), 1702–1725.
Rousselier, G., Luo, M., Mohr, D., 2012. Macroscopic plasticity modeling of anisotropic aluminum extrusions using a reduced texture methodology. Int. J. Plast., 144–165.
Sackett, E., Germain, L., Bache, M., 2007. Crystal plasticity, fatigue crack initiation and fatigue performance of advanced titanium alloys. Int. J. Fatigue 29, 2015–2021.
Segurado, J., Lebensohn, R.A., LLorca, J., Tome, C.N., 2012. Multiscale modeling of plasticity based on embedding the viscoplastic self-consistent formulation in implicit finite elements. Int. J. Plast. 28 (1), 124–140.
Semiatin, S.L., Montheillet, F., Shen, G., Jonas, J.J., 2002. Self-consistent modeling of the flow behavior of wrought alpha/beta titanium alloys under isothermal and nonisothermal hot-working conditions. Metall. Trans. A. 33 (8), 2719–2727.
Sinha, V., Mills, M.J., Williams, J.C., 2004. Understanding the contributions of normal-fatigue and static loading to the dwell fatigue in a near-alpha titanium alloy. Metall. Mater. Trans. A 35, 3141–3148.
Suresh, S., 1998. Fatigue of Materials. Cambridge University Press, Cambridge.
Terada, K., Kikuchi, N., 2001. A class of general algorithm for multi-scale analysis of heterogeneous media. Comput. Meth. Appl. Mech. Eng. 190, 5427–5464.
Tome, C.N., Maudlin, P.J., Lebensohn, R.A., Kaschner, G.C., 2001. Mechanical response of zirconium – I derivation of a polycrystal constitutive law and finite element analysis. Acta Mater. 49, 3085–3096.
Venkataramani, G., Deka, D., Ghosh, S., 2006. Crystal plasticity based FE model for understanding microstructural effects on creep and dwell fatigue in Ti-6242. ASME J. Eng. Mater. Tech. 128 (3), 356–365.
Venkataramani, G., Ghosh, S., Mills, M.J., 2007. A size dependent crystal plasticity finite element model for creep and load-shedding in polycrystalline titanium alloys. Acta Mater. 55, 3971–3986.
Venkataramani, G., Kirane, K., Ghosh, S., 2008. Microstructural parameters affecting creep induced load shedding in Ti-6242 by a size dependent crystal plasticity FE model. Int. J. Plas. 24, 428–454.
Venkatramani, G., Ghosh, S., Mills, M.J., 2007. A size dependent crystal plasticity finite element model for creep and load-shedding in polycrystalline titanium alloys. Acta Mater. 55, 3971–3986.
Watanabe, I., Setoyama, D., Nagasako, N., Iwata, N., Nakanishi, K., 2012. Multiscale prediction of mechanical behavior of ferritepearlite steel with numerical material testing. Int. J. Numer. Meth. Eng. 98, 829–845.
Williams, J.C., Baggerly, R.G., Paton, N.E., 2002. The deformation behavior of hcp Ti-Al alloy single crystals. Metall. Mater. Trans. A 33, 837–850.

Wu, X., Kalidindi, S.R., Necker, C., Salum, A., 2007. Prediction of crystallographic texture evolution and anisotropic stress–strain curves during large plastic strains in high purity α titanium using a Taylor-type crystal plasticity model. Acta Mater. 55, 423–432.
Zhang, M., Zhang, J., McDowell, D.L., 2007. Microstructure-based crystal plasticity modeling of cyclic deformation of Ti6Al4V. Int. J. Plast. 23 (8), 1328–1348.